UNIVERSIDADE FEDERAL DE MINAS GERAIS
Instituto de Ciências Exatas
Programa de Pós-graduação em Física

Daniel Aguiar Pinto

HYDRODYNAMICS OF BUBBLES IN A FIRST-ORDER ELECTROWEAK PHASE TRANSITION

Belo Horizonte
2025

Daniel Aguiar Pinto

HYDRODYNAMICS OF BUBBLES IN A FIRST-ORDER ELECTROWEAK PHASE TRANSITION

Dissertação apresentada ao Programa de Pós-Graduação em Física do Instituto de Ciências Exatas da Universidade Federal de Minas Gerais como requisito parcial para obtenção do título de Mestre em Ciências.

Orientador: Gláuber Carvalho Dorsch

Belo Horizonte

2025

Dados Internacionais de Catalogação na Publicação (CIP)

P659h Pinto, DanielAguiar.
Hydrodynamics of bubbles in a first-order electroweak phase transition/Daniel Aguiar Pinto. –2025.
78f. :il.

Orientador: Gláuber Carvalho Dorsch.
Dissertação (mestrado)– UniversidadeFederal de MinasGerais, Departamento de Física.
Bibliografia:f. 73-78.

1.Cosmologia.2.Transiçãodefase.3.Hidrodinâmica.I.Título.II.Dorsch,Gláuber Carvalho.III. Universidade Federal de Minas Gerais, Departamento de Física.

CDU – 52(043)

Ficha catalográfica elaborada por Romário Martins Ribeiro – CRB6 3595
Biblioteca ProfessorManoel Lopes de Siqueira–Departamento de Física - UFMG

UNIVERSIDADE FEDERAL DE MINAS GERAIS

FOLHA DE APROVAÇÃO

A presente dissertação, intitulada "**Hydrodynamics of bubbles in a first-order electroweak phase transition**" de autoria de **DANIEL AGUIAR PINTO** submetida à Comissão Examinadora, abaixo-assinada, foi aprovada para obtenção do grau de **MESTRE EM FÍSICA, área de concentração Física,** em 09 de abril de 2025.

Belo Horizonte, 09 de abril de 2025.

Prof. Gláuber Carvalho Dorsch
Orientador do estudante
Departamento de Física/UFMG

Prof. Bruce Lehmann Sánchez Vega
Departamento de Física/UFMG

Prof. Mário Sergio Carvalho Mazzoni
Departamento de Física/UFMG

Documento assinado eletronicamente por **Bruce Lehmann Sanchez Vega**, **Membro de comissão**, em 10/04/2025, às 11:47, conforme horário oficial de Brasília, com fundamento no art. 5º do Decreto nº 10.543, de 13 de novembro de 2020.

Documento assinado eletronicamente por **Mario Sergio de Carvalho Mazzoni**, **Membro**, em 10/04/2025, às 12:45, conforme horário oficial de Brasília, com fundamento no art. 5º do Decreto nº 10.543, de 13 de novembro de 2020.

Documento assinado eletronicamente por **Gláuber Carvalho Dorsch**, **Professor do Magistério Superior**, em 11/04/2025, às 11:21, conforme horário oficial de Brasília, com fundamento no art. 5º do Decreto nº 10.543, de 13 de novembro de 2020.

A autenticidade deste documento pode ser conferida no site https://sei.ufmg.br/sei/controlador_externo.php?acao=documento_conferir&id_orgao_acesso_externo=0, informando o código verificador **4115362** e o código CRC **439B3A0A**.

Referência: Processo nº 23072.222337/2025-94 SEI nº 4115362

Acknowledgements

Primeiramente, gostaria de expressar minha profunda gratidão ao meu orientador, Gláuber, que desempenhou um papel central na minha formação como pesquisador. Foram inúmeras reuniões, insights valiosos e novas perspectivas que contribuíram decisivamente para o desenvolvimento de um senso crítico científico mais apurado.

Iniciei minha iniciação científica no quinto período da graduação e, desde então, adquiri conhecimentos e habilidades que certamente serão fundamentais em minha trajetória no doutorado na Universidade de Varsóvia.

Agradeço também à minha família: Fernanda, Zilda (minha querida e saudosa mãe) e meu pai, Fernando. O apoio incondicional de cada um deles foi essencial para que eu chegasse até aqui e concluísse esta dissertação.

Por fim, agradeço aos meus amigos, cuja rede de apoio emocional e os bons momentos compartilhados foram igualmente importantes para tornar esta conquista possível.

This study was financed in part by the Coordenação de Aperfeiçoamento de Pessoal de Nível Superior – Brasil (CAPES) – Finance Code 001.

Resumo

A detecção de ondas gravitacionais (GWs), e a forte evidência de um fundo estocástico de GWs observada pelo NANOGrav, provam que somos capazes de extrair informações anteriormente inacessíveis. Isso nos permite reconstruir eventos que ocorreram há muito tempo e em galáxias distantes. Dentre as possíveis fontes dessas GWs, as transições de fase cosmológicas de primeira ordem desempenham um papel de destaque do ponto de vista da física de partículas.

Nesta dissertação, o assunto central de estudo é entender os efeitos hidrodinâmicos das transições de fase de primeira ordem e calcular a velocidade terminal da parede da bolha durante uma transição de fase cosmológica, modelando efeitos não-equilíbrio no plasma. Um operador ϕ^6 é incluído no potencial efetivo do Modelo Padrão para imitar efeitos de nova física. O aquecimento hidrodinâmico do plasma à frente da bolha é levado em conta.

Nós incluímos termos de ordem superior no chamado "fluido *Ansatz*"-expansão na função distrubuição considerando efeitos fora do equilíbrio- e os comparamos com o *Ansatz* usualmente adotado. Mostramos que essa correção pode até transformar soluções de detonação em deflagrações. Esse resultado também corrobora achados recentes na literatura de que, para um conteúdo de partículas do Modelo Padrão no plasma, apenas soluções de deflagração são viáveis. No entanto, também mostramos que esse resultado pode ser alterado em uma teoria com um conteúdo de partículas diferente.

Para que essa velocidade fosse calculada, todos os parâmetros da transição devem ter sido previamente determinados. Dessa forma, o trabalho estabelece um caminho para obter um conjunto completo de parâmetros necessários no cálculo da amplitude de ondas gravitacionais originadas por transições de fase de primeira ordem.

Palavras-chave: cosmologia;transição de fase electrofraca; potencial efetivo;mecanismo de Higgs.

Abstract

The detection of gravitational waves (GWs), and the strong evidence for a stochastic GW background seen by NANOGrav, prove that we are capable of extracting information previously inaccessible to us allows to reconstruct events that took place a long time ago and in faraway galaxies. Among the possible sources of these GWs, first-order cosmological phase transitions play a prominent role from the perspective of particle physics.

In this dissertation, the central subject of study is to understand the hydrodynamical effects of first-order phase transitions and to compute the terminal bubble wall velocity during a cosmological phase transition by modeling non-equilibrium effects in the plasma. A ϕ^6 operator is included in the Standard Model effective potential to mimic effects of new physics. Hydrodynamical heating of the plasma ahead of the bubble is taken into account.

We include higher order terms in the fluid *Ansatz* - expansion in the distribution function considering out-of-equilibrium effects- and compare it to a simpler *Ansatz* usually adopted in literature. We show that this correction may even turn detonation solutions into deflagrations. This result also corroborates recent findings in the literature that, for a Standard Model particle content in the plasma, only deflagration solutions are viable. However, we also show that this outcome may be altered in a theory with a different particle content.

For this velocity to be calculated, all transition parameters must have been previously determined. Thus, the work also establishes a path to obtain a complete set of parameters required for calculating the amplitude of gravitational waves generated by first-order phase transitions.

Keywords: cosmology;electroweak phase transition;effective potential;higgs mechanism.

Contents

1 Introduction

In the past century, physicists have formulated and refined descriptions of the fundamental laws of nature across large and small scales. The ΛCDM model is a physical theory that successfully describes cosmic expansion, the cosmic microwave background (CMB), and the large-scale structure of the universe.

On the other hand, the Standard Model (SM) of particle physics provides a quantum field theory framework that accurately explains the fundamental forces (except gravity) and elementary particles observed in experiments. The interplay between ΛCDM and the SM remains a crucial frontier in theoretical physics, motivating extensions of both models to achieve a more unified understanding of fundamental interactions and cosmology. The main theme of this thesis will be the connection between the Standard Model and Cosmology, and how gravitational waves can contribute to the search for new physics beyond the energy scales we can probe with current collider experiments.

To understand this connection, let us first consider cosmology. It is a well-known fact in cosmology that there is an inverse relationship between the age of the universe and its temperature [1]. This relationship implies that matter behaved differently at earlier times. Understanding this behavior is key to uncovering the history of our universe. Structures such as galaxies and ourselves could only form once the universe cooled to specific temperature thresholds.

If we trace the history of the cosmos to sufficiently early times, we will see that all matter would become unbound. We would have a plasma of ionized particles, unable to form bound states such as nuclei, atoms, molecules or larger structures. Perhaps more shocking is the fact that also the way these particles interact will change depending on the temperature of this plasma. So the history of the Cosmos can really be divided into eras, as illustrated in figure 1.

At present, the universe is governed by four fundamental interactions: electromagnetism, the weak force, the strong force, and gravity. However, studying the Standard Model at finite temperatures reveals that, prior to $t \sim 10^{-12}$ seconds in the history of the universe, the electromagnetic and weak interactions behaved as a single unified interaction, known as the electroweak interaction.

We can speculate whether, in even earlier epochs, additional unifications occurred, potentially culminating in a description involving only one fundamental interaction. However, these hypothetical unifications remain speculative: the only one that has been empirically tested so far is the electroweak unification. The process of interaction unification is illustrated in Figure 5.

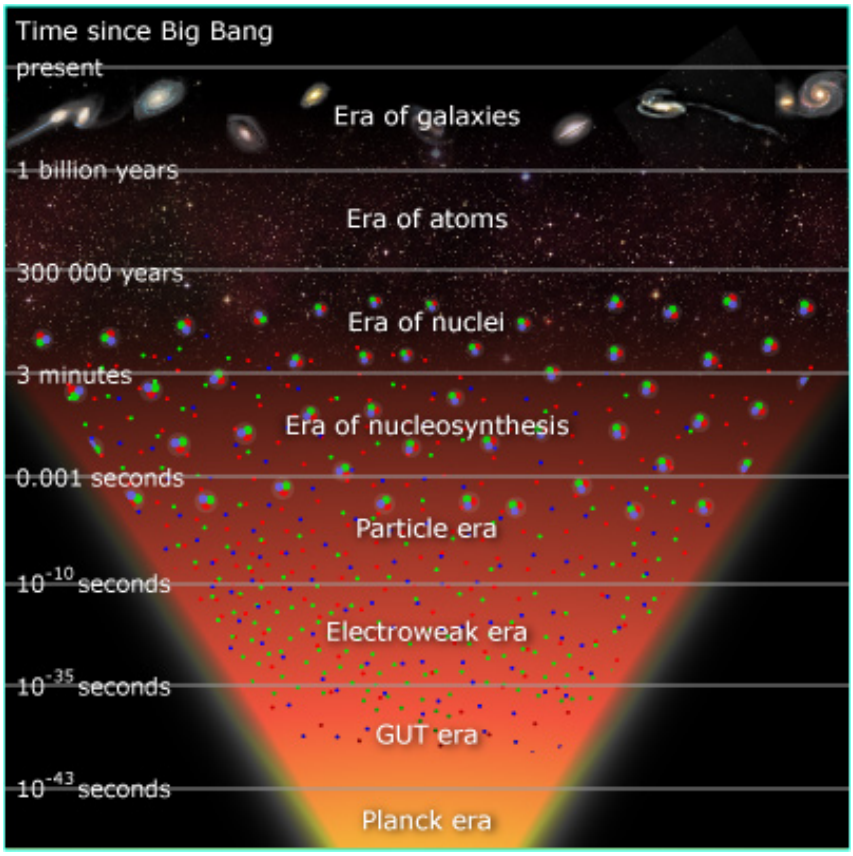

Figure 1 – Eras of particle behavior since the since the origin of the hot plasma. A more complete description of each era can be found in cosmology textbooks [2, 3].

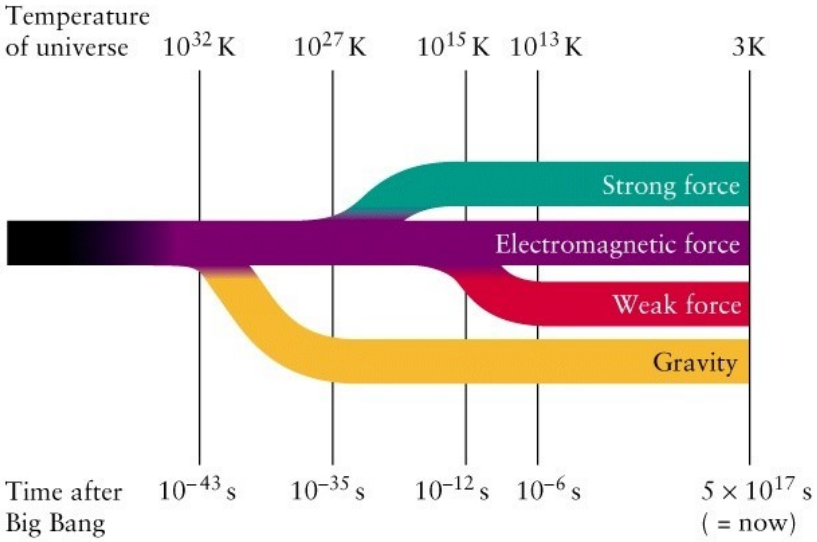

Figure 2 – Eras of interaction behavior since the origin of the hot plasma. While gravity has yet to be described in a quantum paradigm, the Standard Model successfully describes the behavior of the other three interactions.

New insights into fundamental physics are anticipated as we enter the era of gravitational-wave astronomy [4–7]. The detection of gravitational waves (GWs) by

LIGO/Virgo/KAGRA [4–7] and the compelling evidence for a stochastic GW background observed by NANOGrav [8] demonstrate our growing ability to extract information from messengers previously inaccessible. These breakthroughs enable us to reconstruct events that occurred long ago and in distant galaxies.

Among the possible sources of these GWs, first-order cosmological phase transitions hold particular significance for particle physics. Given that the early universe experienced periods of extremely high temperatures, any remnants from such epochs carry valuable information about the effective particle content and the nature of their interactions in this highly energetic regime. A relevant process involves particles in the plasma acquiring mass via the Higgs mechanism [9]. If this happens to occur via a first order phase transition, this process would be analogous to the boiling of water: regions where particles gain mass—referred to as 'bubbles'—form within a massless plasma. During bubble expansion, mechanisms such as baryogenesis and dark matter production could occur. At the end of the transition, the collisions between bubbles disrupt their spherical symmetry, resulting in a time-dependent quadrupole moment in the energy-momentum tensor, generating GWs [10–12], Importantly, these remnants could be detected by the future Laser Inteferometer Spacial Antenna (LISA) [13], which will start taking data in the next decade.

Detecting cosmological GWs could place stringent constraints on particle physics models, provided we have accurate predictions of how the GW spectrum depends on the underlying microphysics. Crucially, the information conveyed by these novel messengers could complement those obtained from collider experiments [14, 15]. Furthermore, such a cosmological phase transition could produce other relics, including a matter-antimatter asymmetry [16, 17] and a dark matter abundance [18–21].

In this dissertation, the central subject of study is to understand the hydrodynamical effects of first-order phase transitions and to compute the terminal bubble wall velocity during a cosmological phase transition by modeling non-equilibrium effects in the plasma with the so-called "extended fluid *ansatz*" [22]. A ϕ^6 operator is included in the Standard Model effective potential to mimic effects of new physics. Hydrodynamical heating of the plasma ahead of the bubble is taken into account. We include higher order terms in the fluid *ansatz* and compare it to the perfect fluid *ansatz* usually adopted. We show that this correction may even turn detonation solutions into deflagrations. This result also corroborates recent findings in the literature that, for a Standard Model particle content in the plasma, only deflagration solutions are viable. However, we also show that this outcome may be altered in a theory with a different particle content.

The dissertation is organized as follows: because this transition occurs at high temperatures and involves microphysical processes, we must delve into quantum field theory (QFT) at finite temperature to understand how the Higgs boson—the central player in this transition—interacts with other particles. This constitutes the focus of the first

chapter, where we describe QFT at a statistical level and use this formalism to compute important thermodynamic properties relevant for the generation of gravitational waves.

The second chapter explores how a gravitational wave experiment, such as LISA, could detect a stochastic GW background. We will compare LISA's sensitivity curves with GW spectra derived from our specific model.

The core of this dissertation lies in the final chapters. One of the most critical and challenging parameters for determining the GW spectrum is still missing: the bubble wall velocity, v_w, which is the primary focus of this work. During the phase transition, the plasma is driven out of equilibrium as particles gain mass. This process demands a sophisticated hydrodynamic treatment of the plasma. We show how the particle content of the theory affects the behavior of the bubble wall velocity, and, ultimately, how this parameter influences the resulting GW power spectrum. Finally, chapter 7 is left to final remarks and conclusions.

2 First-order Electroweak Phase transitions

2.1 Spontaneous Symmetry Breaking

In nature, exact conservation laws are a manifestation of precise symmetries. An exact symmetry in a Lagrangian is characterized by two conditions: the Lagrangian density remains invariant under the symmetry transformation, and the physical vacuum is also invariant under this transformation. While some symmetries, such as flavor symmetries or nuclear isospin, are only approximate, others can be exact.

Modern particle physics is founded on the principle that fundamental interactions adhere to specific exact symmetries. This implies that particles participating in these interactions belong to specific representations of an underlying symmetry group, and any symmetry transformation leaves the theory, particularly the Lagrangian, invariant.

For instance, the electroweak interaction is governed by the symmetry group $\mathrm{SU}(2)_L \times \mathrm{U}(1)_Y$. Particles involved in weak interactions are charged under $\mathrm{SU}(2)_L$, forming non-trivial representations of this group. For example, left-chiral fermions are organized into $\mathrm{SU}(2)_L$ doublets, pairing the charged lepton ℓ (e.g., e^-, μ^-, τ^-) with its corresponding neutrino ν_ℓ. Under the weak interaction, these particles are treated as two states of the same entity. Experimental evidence supports this framework, though the differing masses of charged leptons and neutrinos reveal that these particles are not identical in every respect. While the theory assumes an exact symmetry, the mass differences point to a breaking of this symmetry. This apparent contradiction is resolved through the concept of spontaneous symmetry breaking.

In spontaneous symmetry breaking, the fundamental laws described by the Lagrangian are symmetric under a specific group of transformations (e.g., $\mathrm{SU}(2)_L \times \mathrm{U}(1)_Y$), but the vacuum state (the lowest energy state) is not. In essence, the symmetry governs the dynamics of the particles, but it is not reflected in the vacuum configuration.

To illustrate spontaneous symmetry breaking, we consider a toy model with a real scalar field ϕ. The Lagrangian is given by:

$$\mathcal{L} = \frac{1}{2}(\partial_\mu \phi)(\partial^\mu \phi) - V(\phi), \tag{2.1}$$

where $V(\phi)$ is the potential. If the potential is an even function of ϕ, i.e.,

$$V(\phi) = V(-\phi), \tag{2.2}$$

the Lagrangian is invariant under the parity transformation:

$$\phi \to -\phi. \tag{2.3}$$

Now, consider the specific potential:

$$V(\phi) = \frac{1}{2}\mu^2\phi^2 + \frac{1}{4}|\lambda|\phi^4. \tag{2.4}$$

If $\mu^2 > 0$, the potential has a unique minimum at $\phi = 0$, i.e.,

$$\langle\phi\rangle_0 = 0. \tag{2.5}$$

However, if $\mu^2 < 0$, as shown in Figure 3, the potential develops two new degenerate minima at $\pm v$. While the potential itself remains symmetric under parity ($\phi \to -\phi$), the spontaneous selection of one of these vacua ($+v$ or $-v$) breaks this symmetry . This is a classic example of spontaneous symmetry breaking. The minima are located at:

$$\langle\phi\rangle_0 = \pm\sqrt{-\frac{\mu^2}{|\lambda|}} \equiv \pm v. \tag{2.6}$$

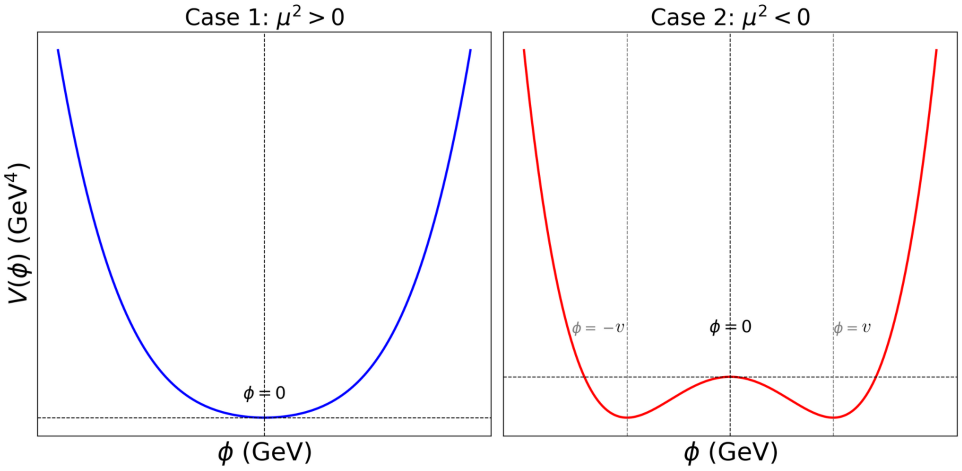

Figure 3 – A scalar field potential illustrating spontaneous symmetry breaking as the parameter changes from $\mu^2 > 0$ to $\mu^2 < 0$.

It is important to emphasize that this example is merely a toy model, and a more accurate description of the Standard Model with real particle content must be introduced.

Let us return to the case of the $SU(2)_L \times U(1)_Y$ symmetry, as found in the Standard Model. As mentioned, the left-chiral fermions belong to $SU(2)L$ doublets, which we can write as

$$L_e \equiv \begin{pmatrix} \nu_e \\ e^- \end{pmatrix}_L, \tag{2.7}$$

where the left-handed states are

$$\nu_L = \frac{1}{2}(1-\gamma_5)\nu \quad \text{and} \quad e_L = \frac{1cx}{2}(1-\gamma_5)e. \tag{2.8}$$

As an approximation to mimic the Standard Model [1], we will consider massless neutrinos, which do not have a right-handed component. Therefore, the right-handed leptonic part is

[1] Here, we are simulating SM because we are not considering the other families of leptons nor quarks

given by

$$R_e = e_R = \frac{1}{2}(1+\gamma_5)e. \tag{2.9}$$

The $U(1)_Y$ hypercharge can be determined using the well-known Gell-Mann–Nishijima relation for the electric charge, given by

$$Q = I_3 + \frac{1}{2}Y, \tag{2.10}$$

where Q represents the electric charge, I_3 is the third component of the weak isospin associated with the $SU(2)_L$ gauge symmetry, and Y is the hypercharge under $U(1)_Y$.

Applying the Gell-Mann–Nishijima relation to each component separately of 2.7, and recalling that the upper component has $I_3 = +1/2$ and the lower has $I_3 = -1/2$, we obtain the hypercharge of the left-handed lepton doublet is $Y_L = -1$.

On the other hand, right-handed leptons are singlets under $SU(2)_L$, meaning they have $I_3 = 0$. The right-handed electron e_R^- satisfies

$$Q(e_R^-) = I_3 + \frac{1}{2}Y_R = 0 + \frac{1}{2}Y_R = -1. \tag{2.11}$$

Solving for Y_R, we find

$$Y_R = -2. \tag{2.12}$$

Furthermore, since hypercharge and weak isospin generators commute, i.e.,

$$[I_3, Y] = 0, \tag{2.13}$$

this ensures that the eigenstates of I_3 remain eigenstates of Y, a necessary condition for maintaining the consistency of the Standard Model gauge structure.

Thus, we conclude that the hypercharges of left- and right-chiral leptons in the Standard Model are

$$Y_L = -1, \quad Y_R = -2. \tag{2.14}$$

Now, to construct a $SU(2)_L \times U(1)_Y$ theory, we define the gauge bosons of $SU(2)_L$ as b_μ^1, b_μ^2, b_μ^3, and for $U(1)_Y$, the gauge boson $\mathcal{A}_\mu$. The Lagrangian for this theory can be written as

$$\mathcal{L} = -\frac{1}{4}F^l_{\mu\nu}F^{l\mu\nu} - \frac{1}{4}f_{\mu\nu}f^{\mu\nu} + \mathcal{L}_{\text{leptons}}, \tag{2.15}$$

where the field strength tensors are

$$F^l_{\mu\nu} = \partial_\nu b^l_\mu - \partial_\mu b^l_\nu + g\epsilon_{jkl}b^j_\mu b^k_\nu \tag{2.16}$$

for $SU(2)L$, and

$$f_{\mu\nu} = \partial_\nu \mathcal{A}_\mu - \partial_\mu \mathcal{A}_\nu \tag{2.17}$$

for $U(1)_Y$. The gauge-covariant derivative is

$$\mathcal{D}_\mu = \partial_\mu + \frac{ig'}{2}\mathcal{A}_\mu Y + \frac{ig}{2}\boldsymbol{\tau}\cdot\mathbf{b}_\mu, \tag{2.18}$$

and therefore, the lepton part of the Lagrangian is given by $(\bar{\Psi} i\gamma^\mu \mathcal{D}_\mu \Psi)$, i.e.,

$$\mathcal{L}_{\text{leptons}} = \overline{\mathrm{R}} i\gamma^\mu \left(\partial_\mu + \frac{ig'}{2}\mathcal{A}_\mu Y\right)\mathrm{R} + \overline{\mathrm{L}} i\gamma^\mu \left(\partial_\mu + \frac{ig'}{2}\mathcal{A}_\mu Y + \frac{ig}{2}\boldsymbol{\tau}\cdot\mathbf{b}_\mu\right)\mathrm{L}, \tag{2.19}$$

where g is the coupling for the weak-isospin group $SU(2)_L$ and the weak hypercharge coupling for $U(1)_Y$ is defined as $g'/2$.

Up to this point, our theory does not align with the real world. It includes four massless bosons and lacks an electron mass term (which would explicitly break the symmetry, since fermion mass terms involve a mixing of left- and right-chiral components, which transform differently under $SU(2)_L$). Therefore, we need to modify the theory to provide mass to the desired particles. To do this, we define the complex doublet of scalar fields as

$$\phi \equiv \begin{pmatrix}\phi^+ & \phi^0\end{pmatrix}, \tag{2.20}$$

and add the familiar scalar part to the Lagrangian,

$$\mathcal{L}_{\text{scalar}} = \left(\mathcal{D}^\mu\phi\right)^\dagger \left(\mathcal{D}_\mu\phi\right) - V\left(\phi^\dagger\phi\right), \tag{2.21}$$

where the potential is given by

$$V(\phi) = \frac{\mu^2}{2}\phi^\dagger\phi + \frac{|\lambda|}{4}(\phi^\dagger\phi)^2. \tag{2.22}$$

We are also free to add an interaction term involving Yukawa couplings of the scalars to the fermions,

$$\mathcal{L}_{\text{Yukawa}} = -\zeta_e\left[\overline{\mathrm{R}}\left(\phi^\dagger \mathrm{L}\right) + \left(\overline{\mathrm{L}}\phi\right)\mathrm{R}\right]. \tag{2.23}$$

Considering again that $\mu^2 < 0$, one can choose the vacuum expectation value (VEV) of the scalar potential as

$$\langle\phi_0\rangle = \begin{pmatrix}0\\ v/\sqrt{2}\end{pmatrix}, \tag{2.24}$$

with v given by

$$v = \sqrt{-\frac{\mu^2}{\lambda}}. \tag{2.25}$$

This symmetry breaking preserves only the $U(1)_{EM}$ symmetry, which is generated by the electric charge. This can be verified by applying the generators of infinitesimal transformations to the vacuum, leading to equation 2.10 when applied to the vacuum expectation value (VEV) $\langle\phi_0\rangle$, keeping the symmetry unbroken. This implies that a linear combination of generators (electric charge) prevents the photon from acquiring mass, while the other gauge bosons necessarily acquire mass.

To analyze this, we expand the Lagrangian of the theory around the VEV to observe the behavior of the oscillations close to this minimum:

$$\phi = \exp\left(\frac{i\zeta\cdot\boldsymbol{\tau}}{2v}\right)\begin{pmatrix}0\\(v+\eta)/\sqrt{2}\end{pmatrix}. \tag{2.26}$$

To simplify the physical interpretation, we explore the gauge invariance and use the so-called unitary gauge:

$$\phi \to \phi' = \exp\left(-i\frac{\zeta\cdot\boldsymbol{\tau}}{2v}\right)\phi = \begin{pmatrix}0\\(v+\eta)/\sqrt{2}\end{pmatrix}, \tag{2.27}$$

where the other fields also undergo this rotation, but $\mathcal{A}_\mu$ and R remain unchanged. We then explicitly expand $\mathcal{L}_{\text{scalar}}$ to highlight the main features of our theory. The new kinetic term in the scalar Lagrangian becomes:

$$D_\mu\phi = \left(\partial_\mu + i\frac{g}{2}\boldsymbol{\tau}\cdot\mathbf{b}_\mu + i\frac{g'}{2}\mathcal{A}_\mu Y\right)\begin{pmatrix}0\\\frac{v+\eta}{\sqrt{2}}\end{pmatrix}. \tag{2.28}$$

For the $SU(2)_Y$ components, this leads to:

$$i\frac{g}{2}\boldsymbol{\tau}\cdot\mathbf{b}_\mu\cdot\phi_0\Big|_{v+\eta} = \frac{ig}{2}\begin{pmatrix}b^3_\mu & b^1_\mu - ib^2_\mu\\ b^1_\mu + ib^2_\mu & -b^3_\mu\end{pmatrix}\cdot\phi_0\Big|_{v+\eta} = \frac{ig}{2}\begin{pmatrix}(b^1_\mu - ib^2_\mu)\frac{v+\eta}{\sqrt{2}}\\ -b^3_\mu\frac{v+\eta}{\sqrt{2}}\end{pmatrix}. \tag{2.29}$$

Defining:

$$W^\pm_\mu = \frac{b^1_\mu \mp ib^2_\mu}{\sqrt{2}}, \tag{2.30}$$

One can write for the charged bosons:

$$(D_\mu\phi)^\dagger (D^\mu\phi) \supset \frac{g^2}{4}\left(W^+_\mu(v+\eta)\right)\left(W^-_\mu(v+\eta)\right). \tag{2.31}$$

For the neutral gauge bosons, we can use equations 2.28 and 2.29 to obtain:

$$(D_\mu\phi)^\dagger D_\mu\phi \supset \frac{1}{4}\left(g'\mathcal{A}_\mu - gb^3_\mu\right)^2\frac{(v+\eta)^2}{2}. \tag{2.32}$$

Finally, the scalar Lagrangian can be written as:

$$\begin{aligned}\mathcal{L}_{\text{scalar}} =& \frac{v^2}{4}\left[g^2(W^+_\mu)(W^\mu-) + \frac{1}{2}\left(g'\mathcal{A}_\mu - gb^3_\mu\right)^2\right]\\ &+ \frac{1}{2}\left(\partial^\mu\eta\right)\left(\partial_\mu\eta\right) + \mu^2\eta^2 + \text{Interaction terms.}\end{aligned} \tag{2.33}$$

Defining the orthogonal combinations, the Z^0 boson is given by:

$$Z_\mu = \frac{-g'\mathcal{A}_\mu + gb^3_\mu}{\sqrt{g^2+g'^2}}, \tag{2.34}$$

and the photon is:

$$A_\mu = \frac{g\mathcal{A}_\mu + g'b^3_\mu}{\sqrt{g^2+g'^2}}, \tag{2.35}$$

which implies that the Z^0 and Ws bosons acquires a mass:

$$M_{Z^0} = \frac{\sqrt{g^2 + g'^2}\, v}{2} = M_W \sqrt{1 + \frac{g'^2}{g^2}}, \tag{2.36}$$

while A^μ remains massless, as expected. The field η^2 also acquires mass from the quadratic term in $\mathcal{L}_{\text{scalar}}$ and represents the Higgs boson. Additionally, within the Yukawa Lagrangian, the electron gains mass via the term $-\zeta_e v/\sqrt{2}$.

Thus, we have schematically achieved the desired particle content of the Standard Model. A full description of this symmetry breaking, including quarks and the other leptons, can be found in [23].

Unfortunately, this approach, even considering quarks and leptons, is unrealistic in the early universe, which is our main focus here. The previous mechanism described represents the Higgs dynamics at zero temperature, which is not the case in the early hot universe. At this period, the universe can be described using Quantum Field Theory at finite temperatures in a thermal environment. In this framework, the total potential changes with temperature due to the interaction of the Higgs field with other particles in the hot universe.

Thermal corrections arise because, at finite temperatures, particles occupy a range of energy states according to the Bose-Einstein or Fermi-Dirac distributions. These distributions depend on the temperature, altering the propagators of the fields and thus modifying the effective potential. The thermal bath effectively provides an additional background field that the Higgs field interacts with, leading to temperature-dependent changes in its potential energy.

Therefore, let us quantitatively discuss these thermal effects.

2.2 Thermal Potential

At high temperatures, the energy distribution of particles is influenced by thermal excitations due to interactions with the Higgs field, making thermal corrections relevant [24].

In the early universe, the population of these enormous numbers of particles is distributed according to thermal statistics, therefore, we must be able to identify the partition function Z, which in quantum field theory at finite temperature is given by the path integral over field ϕ,

$$Z = \int \mathcal{D}\phi e^{-S_E[\phi]}, \tag{2.37}$$

where $S_E[\phi]$is the euclidian action

$$S_E[\phi] = \int_0^\beta d\tau \int_{\mathbf{x}} d^3x \mathcal{L}_E(\phi, \partial_\mu \phi). \tag{2.38}$$

We are using the imaginary-time formalism $t \to i\tau$ to simplify equations, where $\mathcal{L}_E$ means the lagrangian computed also in the imaginary-time.

In this work we will focus on a lagrangian for the scalar field of the form,

$$\mathcal{L} = \frac{1}{2}\partial_\mu\phi\partial^\mu\phi + \frac{\mu^2}{2}\phi^2 - \frac{\lambda}{4}\phi^4 - \frac{1}{8M^2}\phi^6. \tag{2.39}$$

We include here a ϕ^6 operator, which was absent in our previous discussion about the Standard Model Higgs mechanism. This is because this term is introduced in order to encapsulate effects from unknown physics beyond the Standard Model at an energy scale M [25]. Taking $M \to \infty$ recovers the Standard Model (SM).

With the Lagrangian of the field well defined, the euclidean action $S_E[\phi]$ is

$$S_E[\phi] = \int_0^\beta d\tau \int_{\mathbf{x}} d^3x \left[\frac{1}{2}\left((\partial_\tau\phi)^2 + (\nabla\phi)^2\right) + \frac{\mu^2}{2}\phi^2 - \frac{\lambda}{4}\phi^4 - \frac{\phi^6}{8M^2}\right]. \tag{2.40}$$

Substituting the Euclidean action inside equation 2.54 leads to

$$Z = \int \mathcal{D}\phi \, \exp\left\{-\int_0^\beta d\tau \int_{\mathbf{x}} d^3x \left[\frac{1}{2}\left((\partial_\tau\phi)^2 + (\nabla\phi)^2\right) + \frac{\mu^2}{2}\phi^2 - \frac{\lambda}{4}\phi^4 - \frac{\phi^6}{8M^2}\right]\right\}. \tag{2.41}$$

Because of the ϕ^4 and ϕ^6 terms, we deal with a nonfree scalar field theory (SFT), making the full integral really difficult to solve. Fortunately, one can move this interaction problem to a free scalar field case ($V(\phi) \propto \phi^2$) determining the physics of the free field and adding the quartic and order-six terms as perturbations,

$$V(\phi) = V(\phi_0) + \left.\frac{dV}{d\phi}\right|_{\phi_0}\delta\phi + \frac{1}{2}\left.\frac{d^2V}{d\phi^2}\right|_{\phi_0}\delta\phi^2 + \cdots \tag{2.42}$$

And then, one can associate the $\delta\phi^2$ term as an effective mass in a free scalar theory,

$$m_{\text{eff}}^2 = \left.\frac{dV^2}{d\phi^2}\right|_{\phi_0} = \mu^2 + 3\lambda\langle\phi\rangle^2 + \frac{15\langle\phi\rangle^4}{4M^2}. \tag{2.43}$$

As we are dealing with a constant ϕ_0 at a temperature T, expanding the kinetic terms leads to the Euclidean action:

$$S_E[\delta\phi] \approx \frac{1}{2}\int_0^\beta d\tau \int_{\mathbf{x}} d^3x \, \left[\left((\partial_\tau\delta\phi)^2 + (\nabla\delta\phi)^2\right) + m_{\text{eff}}^2\delta\phi^2\right]. \tag{2.44}$$

Now the integration becomes more straightforward, and we are dealing with an effective "non-interactive" case.

To proceed with the action, we perform the Fourier transform of the field $\delta\phi(x,\tau)$. This step is important because of the fact that the field $\delta\phi(x,\tau)$ exhibits periodicity in the imaginary time τ, which is a direct consequence of the finite-temperature statistical mechanics framework. Explicitly, we have,

$$\delta\phi(x,\tau+\beta) = \delta\phi(x,\tau),$$

This periodicity arises from the quantization of energy at finite temperature. When transitioning from the real-time formulation to the imaginary-time formulation (via $\tau = it$), the field must be periodic to respect the statistical requirements of the system in **thermal equilibrium**. This guarantees that the system behaves consistently with the partition function in statistical mechanics.

To solve this periodic boundary condition, one decomposes the field $\delta\phi(x,\tau)$ in terms of discrete modes with frequencies corresponding to the periodicity in τ. These modes are known as the *Matsubara frequencies*, which are defined as

$$\omega_n = \frac{2\pi n}{\beta},$$

where n is an integer, and ω_n is the frequency associated with the mode. The Matsubara frequencies naturally satisfy the periodic boundary condition because they are quantized in integer multiples of $\frac{2\pi}{\beta}$, ensuring the field's periodicity in imaginary time.

This decomposition allows one to express the field in terms of Fourier components that evolve with these Matsubara frequencies. The Fourier expansion of the field $\delta\phi(x,\tau)$ is given by

$$\delta\phi(X) = \delta\phi(x,\tau) = \frac{1}{\sqrt{V\beta}} \sum_K e^{-iK\cdot X} \delta\phi(K) \tag{2.45}$$

$$= \frac{1}{\sqrt{V\beta}} \sum_K e^{i\mathbf{k}\cdot\mathbf{x}} e^{-i(i\omega_n)(-i\tau)} \delta\phi(\omega_n, \mathbf{k}) \tag{2.46}$$

$$= \frac{1}{\sqrt{V\beta}} \sum_K e^{i\mathbf{k}\cdot\mathbf{x}} e^{-i\omega_n\tau} \delta\phi(\omega_n, \mathbf{k}) \tag{2.47}$$

where $\mathbf{k}$ represents the spatial wavevectors, and $\delta\phi(\omega_n, \mathbf{k})$ are the Fourier components of the field. The sum runs over both the wavevectors $\mathbf{k}$ (which correspond to the spatial degrees of freedom) and the Matsubara frequencies ω_n (which correspond to the temporal degrees of freedom). The factor $\frac{1}{\sqrt{V\beta}}$ is a normalization constant that ensures the correct normalization of the field over both space and time. We have that $\sum_K = \sum_{n,\mathbf{k}}$ and V is the three spatial volume.

In the spatial coordinates, to incorporate periodic boundary conditions over finite lenght L_i, we expressed the field in terms of a Fourier series, where each mode k_i corresponds to a discrete momentum component in the x_i-direction, reflecting the physical interpretation of the field as a sum of waves. The periodicity in space, enforced by the finite extent L_i, discretizes the momenta. This is analogous to the temporal case, where β enforces periodicity in τ. In the infinite volume limit ($L_i \to \infty$), the discrete sum over momenta transitions to an integral, reflecting the *continuum of momentum states* in infinite space:

$$\frac{1}{L_i} \sum_{n_i} \to \int \frac{dk_i}{2\pi} \quad \text{as} \quad L_i \to \infty. \quad V = L_1 \cdot L_2 \cdot \cdots \cdot L_d \tag{2.48}$$

Here, $V = L_1 L_2 \cdots L_d$ represents the total spatial volume. Physically, each term in the sum represents a *mode of the field* characterized by a frequency ω_n (energy) and a wavevector $\mathbf{k}$ (momentum).

Now, we can compute explicitly the integrals of the three terms inside 2.44. The first term leads to,

$$\begin{aligned}\int_0^\beta d\tau \int d^3x \left(\partial_\tau \phi\right)^2 &= \int d^4X \frac{1}{V\beta} \sum_K \sum_{K'} \partial_\tau \left[e^{-i\omega_n \tau} e^{i\mathbf{k}\cdot\mathbf{x}} \delta\phi\left(\omega_n, \mathbf{k}\right)\right] \\ &\times \partial_\tau \left[e^{-i\omega_m \tau} e^{i\mathbf{k}'\cdot\mathbf{x}} \delta\phi\left(\omega_m, \mathbf{k}'\right)\right] \\ = \int d^4X \frac{1}{V\beta} \sum_K \sum_{K'} &e^{i(\mathbf{k}+\mathbf{k}')\cdot\mathbf{x}} e^{-i(\omega_n+\omega_m)\tau} \delta\phi\left(\omega_n, \mathbf{k}\right)\left(-i\omega_n\right)\left(-i\omega_m\right)\delta\phi\left(\omega_m, \mathbf{k}'\right).\end{aligned} \tag{2.49}$$

Here we used the reality of the field and also used the standard integrals. Now, we can use the useful relations,

$$\begin{aligned}\int_0^\beta d\tau e^{i(-\omega_n-\omega_m)\tau} &= \beta\delta\left(-\omega_n - \omega_m\right), \\ \int d^3x e^{i(\boldsymbol{k}+\boldsymbol{k}')\cdot x} &= V\delta^3\left(\mathbf{k}+\mathbf{k}'\right),\end{aligned} \tag{2.50}$$

to find:

$$\begin{aligned}\int_0^\beta d\tau \int d^3x \left(\partial_\tau \phi\right)^2 =& \frac{1}{V\beta} \sum_K \sum_{K'} \left[V\delta^3\left(\mathbf{k}+\mathbf{k}'\right)\right] \left[\beta\delta\left(-\omega_n - \omega_m\right)\right] \\ &\times \delta\phi\left(\omega_n, \mathbf{k}\right)\left(-i\omega_n\right)\left(-i\omega_m\right)\delta\phi\left(\omega_m, \mathbf{k}'\right) \\ =& \sum_K \delta\phi\left(\omega_n, \mathbf{k}\right)\omega_n^2 \delta\phi\left(-\omega_n, -\mathbf{k}\right) = \sum_K \omega_n^2 \delta\phi(K)\delta\phi(-K) \\ =& \sum_K \omega_n^2 \delta\phi^*(K)\delta\phi(K).\end{aligned} \tag{2.51}$$

The second and third terms are structurally similar, with the second term involving a spatial momentum factor of $\mathbf{k^2}$, coming from the spatial derivatives, and the third term involving a mass term m^2, which appears from the term without deritivates. Now, the Euclidean action for the scalar perturbation can be written as:

$$S_E[\delta\phi] \approx \frac{1}{2} \sum_n \sum_{\mathbf{k}} \delta\phi(\omega_n, \mathbf{k}) \left(\omega_n^2 + \mathbf{k}^2 + m_{\text{eff}}^2\right) \delta\phi^*(\omega_n, \mathbf{k}). \tag{2.52}$$

Using the properties of the exponential function, the action contributes to the partition function via:

$$\exp(-S_E) = \prod_{\mathbf{k},n} \exp\left[-\frac{1}{2}\left(\omega_n^2 + \mathbf{k}^2 + m_{\text{eff}}^2\right) \delta\phi(\omega_n, \mathbf{k})\delta\phi^*(\omega_n, \mathbf{k})\right]. \tag{2.53}$$

Recalling the partition function definition:

$$Z = \prod_{\mathbf{k},n} \int \mathcal{D}\phi \, \exp\left[-\frac{1}{2}\left(\omega_n^2 + \mathbf{k}^2 + m_{\text{eff}}^2\right) \delta\phi(\omega_n, \mathbf{k})\delta\phi^*(\omega_n, \mathbf{k})\right], \tag{2.54}$$

the Gaussian integral over the field fluctuations can be evaluated using the standard identity:

$$\int d^D y \, \exp\left(-\frac{1}{2}\vec{y}\cdot\hat{A}\vec{y}\right) = (2\pi)^{D/2}(\det\hat{A})^{-1/2}. \tag{2.55}$$

This is the generalization of the Gaussian integral. Applying this to equation 2.54, we are left with a factor of $(2\pi)^{D/2}$, which is irrelevant because we are taking the logarithm of Z and are interested in the free energy of the system, which can be freely redefined by addition or subtraction of constants. Therefore, the logarithm of Z becomes:

$$\ln Z = \ln \prod_{\mathbf{k},n} \left(\omega_n^2 + \mathbf{k}^2 + m_{\text{eff}}^2\right)^{-1/2} = -\frac{1}{2}\sum_{\mathbf{k},n} \ln\left(\omega_n^2 + \mathbf{k}^2 + m_{\text{eff}}^2\right). \tag{2.56}$$

The sum over the momenta $\mathbf{k}$ will be performed in the end when we take the thermodynamical limit (ie. $V \to \infty$). The challenging part is evaluating the sum over Matsubara frequencies ω_n. Substituting $\omega = i\omega_n = k_0$, the summation becomes:

$$T\sum_n \ln\left(\omega_n^2 + \mathbf{k}^2 + m_{\text{eff}}^2\right) = T\sum_{k_0} \ln\left(-k_0^2 + \mathbf{k}^2 + m_{\text{eff}}^2\right). \tag{2.57}$$

Expanding the logarithm, we obtain:

$$T\sum_{k_0} \ln\left(-k_0^2 + \mathbf{k}^2 + m_{\text{eff}}^2\right) = T\sum_{k_0} \left[\ln\left(\omega_k - k_0\right) + \ln\left(\omega_k + k_0\right)\right], \quad k_0 = \omega_n \tag{2.58}$$

where $\omega_k = \mathbf{k} + m_{\text{eff}}^2$. To compute the first term, the key idea is to rewrite the discrete sum over Matsubara frequencies as a contour integral in the complex plane. To achieve that, one can explore the hyperbolic cotangent function [24], defined as:

$$\coth\left(\frac{\beta k_0}{2}\right), \tag{2.59}$$

which is particularly useful because its poles are located precisely at the Matsubara frequencies. The residue theorem can be employed to compute the sum:

$$T\sum_{k_0} \ln\left(\omega_k - k_0\right) = T\sum_{k_0} \ln\left(\omega_k - k_0\right) \text{Res}\left[\frac{\beta}{2}\coth\left(\frac{\beta k_0}{2}\right)\right]. \tag{2.60}$$

The remaining terms can be treated in a similar manner. By applying the residue theorem and contour integration, the summation simplifies significantly. This follows directly from the theorem:

$$\oint_C f(z)\, dz = 2\pi i \sum \text{Res}\left(f, z_k\right). \tag{2.61}$$

The key idea is to transform the original discrete sum into a contour integral that encircles the poles of the function, allowing us to evaluate it via the residue theorem. Figure 4 illustrates the poles of the coth function, along with the chosen integration contour that will be used.

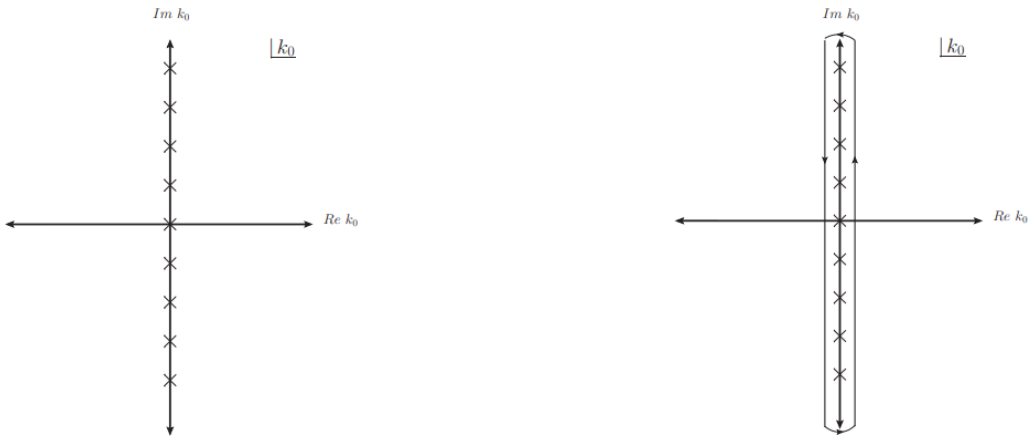

Figure 4 – Poles of $\coth(\beta k_0/2)$ in the left figure and the right figure the path used to encapsulate the residues.

The poles in figure 4 can be described as,

$$\coth\left(\frac{\beta k_0}{2}\right) = \coth(n\pi i) \Rightarrow k_0 = \frac{2\pi i n}{\beta} = i\omega_n, \tag{2.62}$$

with residues $2/\beta$. The residue $\mathrm{Res}\left[\frac{\beta}{2}\coth\left(\frac{\beta k_0}{2}\right)\right]$ evaluates to unity. Using the residue theorem in reverse, the sum over residues can be rewritten as a contour integral. This integral is taken over a path C that encloses the poles of the function dependent on k_0, but excludes the poles of the hyperbolic cotangent ($k_0 = i\omega_n = 2\pi i T$):

$$T\sum_{k_0}\frac{1}{T}\,\mathrm{Res}\left[\ln\left(\omega_k - k_0\right)\frac{\beta}{2}\coth\left(\frac{\beta k_0}{2}\right)\right] = \frac{1}{2\pi i}\oint_{C_1\cup C_2} dk_0\frac{1}{T}\ln\left(\omega_k - k_0\right)\frac{1}{2}\coth\left(\frac{\beta k_0}{2}\right). \tag{2.63}$$

Applying this formula to the first term yields:

$$\begin{aligned} T\sum_{k_0}\frac{1}{T}\ln\left(\omega_k - k_0\right) &= \frac{1}{2\pi i T}\oint dk_0\ln\left(\omega_k - k_0\right)\frac{1}{2}\coth\left(\frac{\beta k_0}{2}\right) \\ &= -\frac{1}{4\pi i T}\oint dk_0\left(\frac{-1}{\omega_k - k_0}\right)\int dk_0\coth\left(\frac{\beta k_0}{2}\right) \\ &= \frac{1}{4\pi i T}\oint dk_0\left(\frac{1}{\omega_k - k_0}\right)\frac{2}{\beta}\ln\left[\sinh\left(\frac{\beta k_0}{2}\right)\right]. \end{aligned} \tag{2.64}$$

Now we have,

$$T\sum_{k_0}\frac{1}{T}\ln\left(\omega_k - k_0\right) = \frac{1}{2\pi i}\oint dk_0\left(\frac{1}{\omega_k - k_0}\right)\ln\left[\sinh\left(\frac{\beta k_0}{2}\right)\right], \tag{2.65}$$

that can be solved using directly the residue theorem, leading to,

$$\frac{1}{2\pi i}\oint dk_0\left(\frac{1}{\omega_k - k_0}\right)\ln\left[\sinh\left(\frac{\beta k_0}{2}\right)\right] = \ln\left[\sinh\left(\frac{\beta\omega_k}{2}\right)\right]. \tag{2.66}$$

Similarly, for the second term, choosing the opposite contour as the first one, we get:

$$T\sum_{k_0}\ln\left(\omega_k + k_0\right) = \ln\left[\sinh\left(\frac{\beta\omega_k}{2}\right)\right]. \tag{2.67}$$

Thus, the sum from Equation 2.60 can be written as:

$$\begin{aligned} T\sum_n \frac{1}{T}\ln\left(\omega_n^2+\omega_k^2\right) &= 2\ln\left[\sinh\left(\frac{\beta\omega_k}{2}\right)\right] \\ &= 2\ln\left[\frac{1}{2}e^{\frac{\beta\omega_k}{2}}\left(1-e^{-\beta\omega_k}\right)\right] \\ &= \beta\omega_k - 2\ln 2 + 2\ln\left(1-e^{-\beta\omega_k}\right). \end{aligned} \tag{2.68}$$

The constant $\ln 2$ can be neglected, as it is independent of temperature. The free energy for a free scalar field can be obtained using the thermodynamic identity:

$$F = -T\ln\mathcal{Z} = T\sum_k\left[\frac{\beta\omega_k}{2} + \ln\left(1-e^{-\beta\omega_k}\right)\right]. \tag{2.69}$$

and then, in the thermodynamic limit, we arrive at the free energy density,

$$f = p = \lim_{V\to\infty} -T\frac{\ln\mathcal{Z}}{V} = -T\ln\mathcal{Z} = T\int\frac{d^3k}{(2\pi)^3}\left[\frac{\beta\omega_k}{2} + \ln\left(1-e^{-\beta\omega_k}\right)\right]. \tag{2.70}$$

It is important to emphasize that this result represents only the dominant term in the expansion of equation 2.42. Including the contributions from all particles in the Standard Model, and also summing the fermion contribution (similar computation), the total thermal contribution is given by:

$$\begin{aligned} \bar{V}_1^{\beta}(\phi,T) = &-\sum_F \frac{g_F T^4}{2\pi^2}\int_0^\infty dx\, x^2 \ln\left(1+e^{-\sqrt{x^2+\beta^2 m_F^2}}\right) \\ &+\sum_B \frac{g_B T^4}{2\pi^2}\int_0^\infty dx\, x^2 \ln\left(1-e^{-\sqrt{x^2+\beta^2 m_B^2}}\right). \end{aligned} \tag{2.71}$$

After integrating the zero-temperature one-loop contribution using a cutoff Λ [26], we obtain the famous Coleman-Weinberg term:

$$\sum_i \frac{g_i}{64\pi^2}\frac{m_i^4}{v^4}\phi^4\ln\frac{\phi^2}{v^2}. \tag{2.72}$$

By adjusting the quadratic and quartic terms to ensure the correct minima at $v = 246.22$ GeV, the total effective potential can be written as:

$$V_{\text{eff}}(\phi,T) = -\frac{\mu^2}{2}\phi^2 + \frac{\lambda}{4}\phi^4 + \frac{\phi^6}{8M^2} + \left(\sum_i \frac{g_i}{64\pi^2}\frac{m_i^4}{v^4}\right)\phi^4\ln\frac{\phi^2}{v^2} + \bar{V}_1^{\beta}(\phi,T), \tag{2.73}$$

where the parameters μ^2 and λ are given by:

$$\mu^2 = \frac{m_h^2}{2} - \frac{3v^4}{4M^2}, \quad \lambda = \frac{m_h^2}{2v^2} - \frac{3v^2}{4M^2}. \tag{2.74}$$

In section 6 we will perform a two-fold analysis to evaluate the impact of the particle content of the theory on the wall velocity. In one case, we will consider only top quarks as heavy particles running in the loop. In the other case, we will consider top quarks, W bosons, and Z bosons running in the loop, with $g_i = 12$, 6, and 3 representing their respective degrees of freedom and masses $m_i = 173.1$ GeV, 80.385 GeV, and 91.1876 GeV, respectively. A clear shape of our potential can be seen in figure 5, where one can see the important critical temperature T_c i.e, the temperature at which we have degenerate minima and the lowest energy state changes discontinuously.

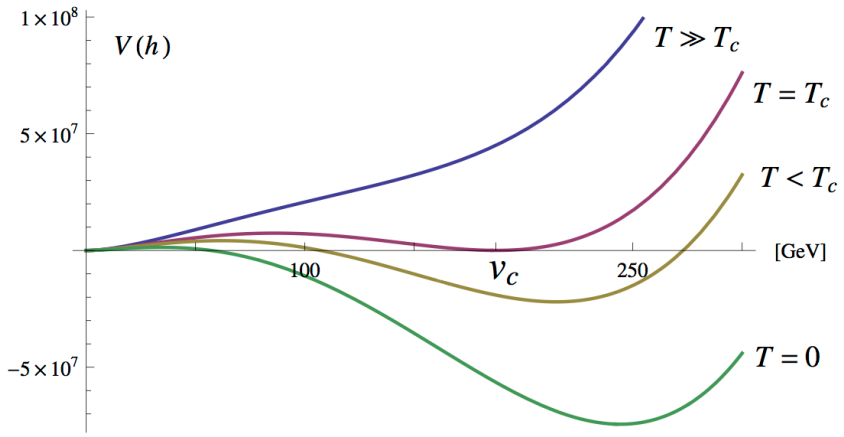

Figure 5 – Higgs effective potential $V_{eff}(\phi, T)$ showing it profile above, at and below critical temperature T_c

To accurately describe a transition that could generate detectable gravitational waves (GWs), it is important to define the types of transitions more precisely. Three types of phase transitions can be defined [27]:

1. **First-order phase transition**: In this case, the order parameter ϕ_0 undergoes a discontinuous change at the critical temperature T_c, which is the temperature at which the minima of the potential are degenerate. Additionally, there is a release of latent heat and a discontinuity in the thermodynamic enthalpy $\omega = T\frac{\partial p}{\partial T}$ at T_c.

2. **Second-order phase transition**: Here, all parameters change continuously at T_c, with no discontinuity in the order parameter or in the thermodynamic quantities.

3. **Crossover**: In this case, the order parameter changes continuously at T_c, but not analytically. This scenario represents a smooth transition without a sharp distinction between the symmetric and broken phases.

A transition with this potential, if of first-order, would occur analogously to water boiling: regions of space appear where particles acquire mass (a probabilistic event that involves surpassing a barrier of the free energy that connects the two minima) - the so-called“bubble” – immersed in the middle of particles that are not yet massive. Then, these nucleated bubbles start a fast percolation. This process can be understood in a pictorial way using figure 6,

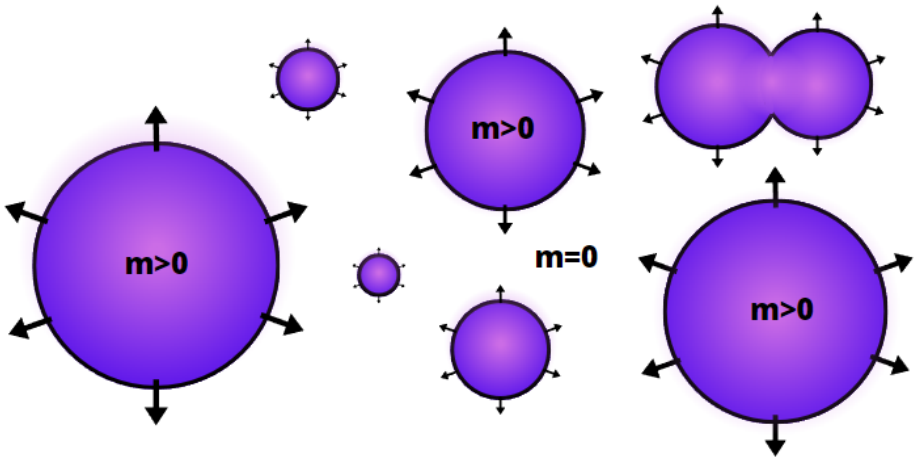

Figure 6 – Bubbles of a First-order phase transition (FOPT) immersed in the region with massless particles

2.3 Nucleation temperature

As mentioned in the previous section, a key parameter of the phase transition is the critical temperature, shown in Figure 5. This temperature corresponds to the point where the potential's minima become degenerate. However, it does not mark the onset of the phase transition. Instead, the transition begins at the nucleation temperature, a temperature below T_c, at which bubbles start to form, which will be discussed next.

First-order electroweak phase transitions proceed via the nucleation of bubbles from a metastable false vacuum state [28], overcoming the potential barrier depicted in Figure 5. Due to surface tension and internal pressure, larger bubbles tend to expand and percolate, while smaller ones collapse, restoring the symmetric phase.

The critical field configurations that mediate the transition between the false and true vacua are known as bounce solutions—solutions to the equations of motion derived from the Euclidean action. The phase transition occurs when the nucleation rate per unit volume surpasses the expansion rate of the universe. In other words, we require the nucleation process to dominate over the rate at which bubbles form and disappear.

To quantify this, we first compute the probability of overcoming the barrier. This can occur via thermal fluctuations or quantum tunneling [2]. In our case, since we are in a high-temperature regime, thermal fluctuations dominate.

For the system to transition to the true vacuum, it must overcome the potential barrier. This requires a fluctuation with energy at least equal to the barrier height, which we denote as E_{sph}. The probability of a local fluctuation of the field ϕ with energy E follows a Boltzmann distribution:

$$P(E) \simeq e^{-E/T} \tag{2.75}$$

Thus, the total probability of overcoming the barrier is given by summing over all possible intermediate configurations with $E > E_{\text{sph}}$:

$$P \simeq \sum_{E>E_{\text{sph}}} e^{-E/T} \tag{2.76}$$

Since we are dealing with static field configurations, the energy of a given configuration $\phi(\mathbf{x})$ is

$$E[\phi] = \int d^3x \left[\frac{1}{2}(\nabla\phi)^2 + V(\phi)\right]. \tag{2.77}$$

The probability of a transition mediated by a fluctuation with energy E is exponentially suppressed by the ratio E/T. Consequently, the dominant contribution to (2.76) comes from the configuration with the lowest possible energy, known in the literature as the sphaleron.

Moreover, this fluctuation corresponds to a bubble mediating the transition between the two minima of the potential. That is, inside the bubble, we have the broken phase, while outside, the system remains in the symmetric phase. Consequently, it must satisfy the boundary conditions:

$$\phi(r \to \infty) = 0 \quad \text{and} \quad \left.\frac{d\phi}{dr}\right|_{\phi=0} = 0. \tag{2.78}$$

Thus, determining the sphaleron solution reduces to an optimization problem: finding the field configuration that minimizes the energy while satisfying these boundary conditions. Applying the Euler-Lagrange equation to this system gives

$$\frac{d}{dr}\left(r^2\frac{d\phi}{dr}\right) - r^2\frac{\partial V}{\partial\phi} = 0, \tag{2.79}$$

which simplifies to

$$\frac{d^2\phi}{dr^2} + \frac{2}{r}\frac{d\phi}{dr} - \frac{\partial V}{\partial\phi} = 0. \tag{2.80}$$

Solving this equation of motion determines the profile $\phi(r)$ that minimizes E and contributes dominantly to (2.76).

For a one-dimensional potential, the solution can be obtained using a shooting method that satisfies the boundary conditions $(d\phi/dr)|_{r=0} = \phi_0$ and $\lim_{r\to\infty} \phi = 0$, leading to a temperature-dependent profile $\phi(r)$. Our goal is to find the temperature at which

$$\frac{\Gamma}{\mathcal{V}} \sim H^4.$$

This nucleation rate is proportional to the probability obtained earlier, and dimensional analysis leads to

$$\frac{\Gamma}{\mathcal{V}} \sim T^4 e^{-E_{\text{sph}}/T}. \tag{2.81}$$

Setting this equal to the Hubble rate to the fourth power, as given by the Friedmann equation,

$$\left(\frac{\dot{a}}{a}\right)^2 = \frac{\pi^2 g^* T^4}{90 M_{\text{Pl}}^2}, \tag{2.82}$$

and substituting into our nucleation rate, we obtain

$$T^4 e^{-E_{\text{sph}}/T} = \left(\frac{\pi^2 g^* T^4}{90 M_{\text{Pl}}^2}\right)^2. \tag{2.83}$$

Applying this condition to the relevant energy scale ($T \approx 100$ GeV) yields a constraint on the nucleation temperature, given by $S(T)/T \approx 140$. A numerical solver is then required to find the profile that satisfies $S_E(T)/T \approx 140$ and thus determines the nucleation temperature T_n.

One can plot a bounce profile at T_n and $M = 700$ GeV in figure 7 to demonstrate bubbles shape. The profile shape in figure 7 is already computed at T_n and evaluating

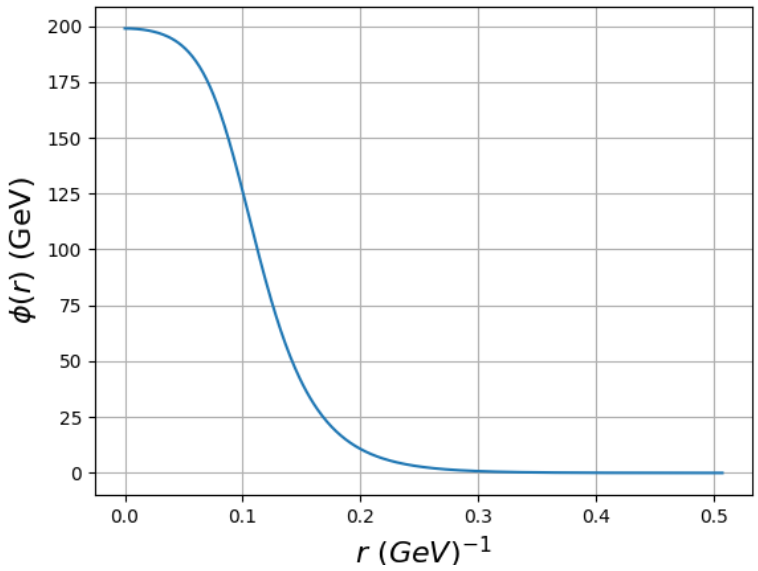

Figure 7 – $\phi(r)$ bubble's shape for T_n starting at ϕ_0.

its integral using 2.77 gives us the desired result of $S_E(T)/T \approx 140$ for nucleation. We

choose an arbitrary value for M but there are regions of M in which the transition never nucleate, called metastable regions.

2.3.1 Additional parameters

We know from the previous discussion that the bubble rate is given by the equation 2.81. With that, one can define the inverse time duration of the transition,

$$\beta \approx \frac{\dot{\Gamma}}{\Gamma} \tag{2.84}$$

with leads to another important parameter, the ratio β/H_*, with H_* Hubble parameter at the temperature T_* (temperature of production of GWs, for our setup it is reasonable to assume $T_* \approx T_n$ [29]). The gravitational wave spectrum is inversely proportional to $(\beta/H_*)^2$ [13], showing a great impact on the spectrum. Now, a key parameter that we are going to use with a certain frequency is the vacuum-released energy normalized with the radiation energy,

$$\alpha = \frac{\rho_{vac}}{\rho^*_{rad}}. \tag{2.85}$$

We again are in a radiation-dominated era and $\rho^*_{rad} = g_*\pi^2 T_*^4/30$. ρ_{vac} can be easily computed using the difference between the two states ie., $\rho_{vac} = \Delta V - 1/4 \cdot T \cdot \Delta(dV/dT)$. We used here the definition of the strength of the phase transition using the trace of the energy momentum tensor [30].

3 Gravitational Waves

3.1 Detection of Gravitational Waves

Gravitational waves are among the most challenging predictions of General Relativity test experimentally, due to the extreme precision required. For instance, consider the perturbation caused by gravitational waves from a binary black hole system, where each black hole has a mass of 10 solar masses and the system is located at a distance on the order of 100 Mpc. The amplitude of the gravitational waves can be measured using the definition of strain $\Delta L/L$, or the length driven from equilibrium δL. For this detection from black hole mergers, this relative displacement was of $\mathcal{O}$ 10^{-21} m [31].

Achieving such precision is a difficult task, and this experimental challenge became particularly evident when gravitational waves were first directly detected in 2015 [8]. However, despite the difficulty, investing effort, time, and resources in this endeavor was justified, as previous successes of General Relativity and indirect evidence of gravitational waves had already been observed in the Hulse-Taylor binary system [32], where the loss of kinetic energy due to gravitational wave emission was measured.

It is noted that interferometric techniques offer the greatest prospects for GW registration due to their high sensitivity and extremely wide frequency band [33]. Therefore, let us try to understand the most straightforward version of this kind of experiment.

3.1.1 An example of a simple Michelson interferometer

Interferometers provide an elegant solution to the experimental challenge of detecting gravitational waves. While they may appear simple at first glance, large gravitational wave interferometers are extremely complex, with numerous degrees of freedom that must be controlled with high precision. Due to this complexity, we will focus on the simplest case, which does not capture the full complexity of a real interferometer.

The Michelson interferometer, used in the Michelson-Morley experiment, is a highly precise system designed to measure changes in the travel time of light along its arms. A conceptual schematic of the system is shown in Figure 8. The setup consists of a laser directed at a beam splitter, which reflects the laser beam with equal probability toward two mirrors. When the light returns, it is split again, and part of it is directed to a light detector.

Let $k_L = \frac{\omega_L}{c}$ and $\lambda_L = \frac{2\pi}{k_L}$ represent the wave properties of light. A spatial component of the electric field of the laser beam leaving the beam splitter can be written

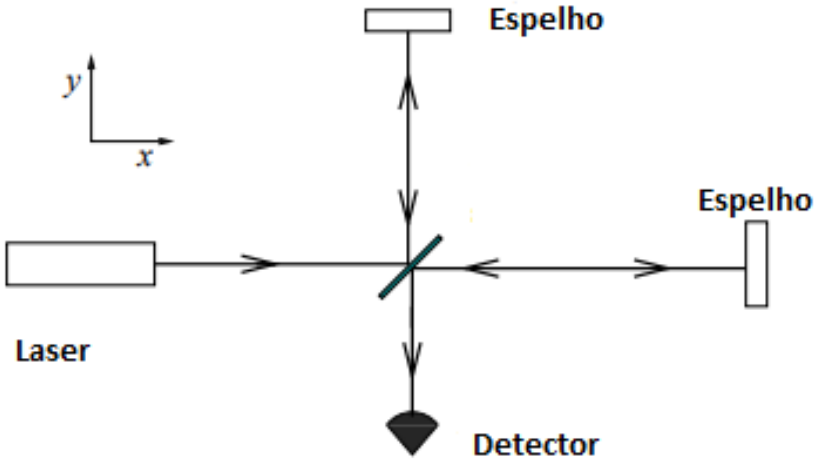

Figure 8 – Simple experiment of the Michelson interferometer.

as

$$E_0 e^{-i\omega_L t + i\vec{k}\cdot\vec{x}}. \tag{3.1}$$

Consider L_x and L_y as the lengths of the two arms, oriented as shown in Figure 8. The power measured by the detector can be calculated, and after some calculation, the eletric field of the laser can be described by,

$$|E_{\text{final}}|^2 = E_0^2 \sin^2[k_L(L_y - L_x)]. \tag{3.2}$$

Thus, any variation in the length of the arms corresponds to a change in the power detected, which is the basis for detecting gravitational waves.

To further explore the calculation, we can use the results of the transverse and traceless gauge transformation discussed in [31] to understand the operation of the interferometer.

In this coordinate system, let us consider objects in free fall. Even in the presence of gravitational waves, the coordinates of these objects remain unchanged. However, it is important to note that although the mirrors of terrestrial interferometers are not in free fall, the forces acting on them are static compared to the frequencies of gravitational waves [34]. Therefore, we can treat the mirrors as if they were in free fall in the horizontal plane.

For simplicity, assume that the gravitational waves only have positive polarization in the z direction (with respect to the coordinate system in Figure 8). In the $z = 0$ plane, we have

$$h_+(t) = h_0 \cos(\omega_{\text{gw}} t). \tag{3.3}$$

From the perturbation of the background Minkowski metric (caused by the GWs),

$$g_{\mu\nu} = \eta_{\mu\nu} + h_{\mu\nu} \tag{3.4}$$

we see that the metric will take the following form (we are in a plane in the TT gauge):

$$g_{\mu\nu} = \begin{pmatrix} -c^2 & 0 & 0 & 0 \\ 0 & 1+h_+(t) & 0 & 0 \\ 0 & 0 & 1-h_+(t) & 0 \\ 0 & 0 & 0 & 1 \end{pmatrix}. \tag{3.5}$$

Since photons travel along null geodesics, setting $ds^2 = 0 = g_{\mu\nu}dx^\mu dx^\nu$ in the metric (3.5), we have:

$$dx = \pm c dt \sqrt{1+h_+(t)} \tag{3.6}$$

and treating h_+ perturbatively,

$$dx = \pm c\, dt \left(1 - \frac{1}{2}h_+(t)\right), \tag{3.7}$$

where + corresponds to the outgoing photon (before reflected) and − to the incoming photon after reflection. After some **boring** calculations involving the time it takes for each laser to travel from the beam to the perturbed arms [34], the resulting effect depends on the change in the phase of each beam. This phase change translates into an observable result in the power $P = |E_{\text{tot}}|^2$ at the final detector. To maximize the observed effect, it can be shown that the arms lengths L_x, L_y (which are equal to cancel noise) should be:

$$L = \frac{L_x + L_y}{2} = \frac{\lambda_{\text{gw}}}{4}.$$

This configuration maximizes the effect. However, the wavelength of gravitational waves is extremely long, making arms of this magnitude impractical due to funding and engineering constraints. A solution to this limitation is provided by the use of Fabry-Perot cavities, which allow the laser to bounce within the cavity, simulating a longer effective length in the interferometer [35].

3.2 Contributions to the Gravitational Wave Spectrum

As discussed in chapter 2, among the possible sources of these GWs, first-order cosmological phase transitions play a prominent role from the perspective of particle physics. Now, with a more solid idea of how an experiment could detect gravitational waves coming from this type of source, we can move on to compute the amplitude of gravitational waves generated by first-order phase transitions.

Three processes contribute to the production of gravitational waves (GWs) during a first-order phase transition. These processes will be discussed sequentially:

- **Scalar field contribution**

This contribution arises from the collision of bubble walls in the plasma. It can be computed using the envelope approximation [13], where a fraction of the latent heat from the phase transition is deposited in a thin shell near the bubble front. The energy in each shell is quickly dispersed after colliding with another shell. This process is illustrated in figure 9. Numerical simulations using this approximation [37] lead to the spectrum:

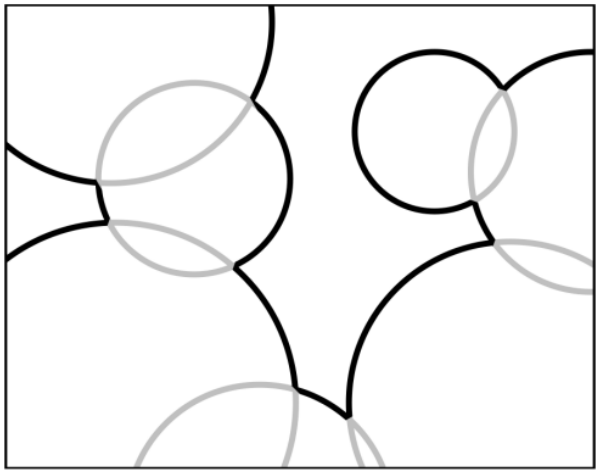

Figure 9 – The collided walls, denoted by the gray lines, gradually lose their energy and momentum densities after collisions [36].

$$h^2\Omega_{\rm env}(f) = 1.67\times10^{-5}\left(\frac{H_*}{\beta}\right)^2\left(\frac{\kappa\alpha}{1+\alpha}\right)^2\left(\frac{100}{g_*}\right)^{1/3}\left(\frac{0.11v_w^3}{0.42+v_w^2}\right)S_{\rm env}(f), \tag{3.8}$$

where $S_{\rm env}(f)$ parametrizes the spectral shape of the GW radiation using the envelope approximation:

$$S_{\rm env}(f) = \frac{3.8(f/f_{\rm env})^{2.8}}{1+2.8(f/f_{\rm env})^{3.8}}, \tag{3.9}$$

with:

$$f_{\rm env} = 16.5\times10^{-3}\,{\rm mHz}\frac{f_*}{\beta}\frac{\beta}{H_*}\frac{T_*}{100\,{\rm GeV}}\left(\frac{g_*}{100}\right)^{1/6}, \tag{3.10}$$

and:

$$f_*/\beta = \frac{0.62}{1.8-0.1v_w+v_w^2}. \tag{3.11}$$

- **Sound Waves**

The expansion of bubble walls generates motion in the plasma, creating sound waves. This type of GW production is an active area of research, and a definitive model that accounts for v_w is not yet available. It turns out that v_w is a crucial parameter for determining the GW spectrum. For generic values of v_w significantly different from the sound speed c_s, numerical results from [38] are fitted by:

$$h^2\Omega_{\rm SW}(f) = 2.65\times10^{-6}\left(\frac{H_*}{\beta}\right)\left(\frac{\kappa_v\alpha}{1+\alpha}\right)^2\left(\frac{100}{g_*}\right)^{1/3} v_w S_{\rm SW}(f), \tag{3.12}$$

where κ_v is the fraction of latent heat transformed into the bulk motion of the fluid [13]. S_{SW} is given by

$$S_{\rm sw}(f) = (f/f_{\rm sw})^3\left(\frac{7}{4+3\,(f/f_{\rm sw})^2}\right)^{7/2}, \tag{3.13}$$

with,

$$f_{\rm sw} = 1.9\times10^{-2}{\rm mHz}\frac{1}{v_w}\left(\frac{\beta}{H_*}\right)\left(\frac{T_*}{100{\rm GeV}}\right)\left(\frac{g_*}{100}\right)^{\frac{1}{6}} \tag{3.14}$$

- **Magnetohydrodynamic (MHD) Contribution**

The expansion of bubbles induces turbulence in the plasma, which in turn generates a time-dependent quadrupole moment in the energy-momentum tensor, producing GWs. Assuming turbulence, as proposed in [39], the contribution to the GW spectrum is given by

$$h^2\Omega_{\rm turb}(f) = 3.35\times10^{-4}\left(\frac{H_*}{\beta}\right)\left(\frac{\kappa_{\rm turb}\alpha}{1+\alpha}\right)^{1/2}\left(\frac{100}{g_*}\right)^{1/3} v_w S_{\rm turb}(f), \tag{3.15}$$

where $\kappa_{\rm turb}$ is the fraction of latent heat transformed into turbulence. There is so far no appropriate modeling for this parameter. It is sometimes assumed that $\kappa_{\rm turb} = \varepsilon\kappa_{\rm sw}$, with typical values ranging from $5-10\%$ [13]. Sometimes extreme cases as $\varepsilon = 0$ (negligible turbulence) [40] and $\varepsilon = 1$ [41] are also assumed. In our case, we are going to assume $\kappa_{\rm turb} = 0.05$.

Therefore, $S_{turb}(f)$ is given by,

$$S_{\rm turb}\,(f) = \frac{(f/f_{\rm turb}\,)^3}{[1+(f/f_{\rm turb}\,)]^{\frac{11}{3}}\,(1+8\pi f/h_*)} \tag{3.16}$$

with,

$$f_{\rm turb}\ = 2.7\times10^{-2}{\rm mHz}\frac{1}{v_w}\left(\frac{\beta}{H_*}\right)\left(\frac{T_*}{100{\rm GeV}}\right)\left(\frac{g_*}{100}\right)^{\frac{1}{6}}, \tag{3.17}$$

and,

$$h_* = 16.5\cdot10^{-3}(T_*/100)(g_*/100)^{1/6}{\rm mHz}. \tag{3.18}$$

These processes contribute to the total spectrum of the stochastic GW background. Each contribution is additive, thus

$$h^2\Omega_{\rm GW} \approx h^2\Omega_{\rm env} + h^2\Omega_{\rm SW} + h^2\Omega_{\rm turb}. \tag{3.19}$$

3.3 LISA

Ground-based interferometers are limited to frequencies above about 10 Hz due to seismic and Newtonian noise. This type of seismic noise affects the interferometer in the form of surface waves, which cause oscillations in the interferometer's suspension mechanisms. On the other hand, Newtonian noise refers to fluctuations in the gravitational force caused by the movement of objects, resulting in variations in the gravitational attraction. The main contribution to this noise comes from seismic noise, which causes variations in mass density and, consequently, fluctuations in the gravitational force. The figure 10 shows different types of noises that can be found in an interferometer [34].

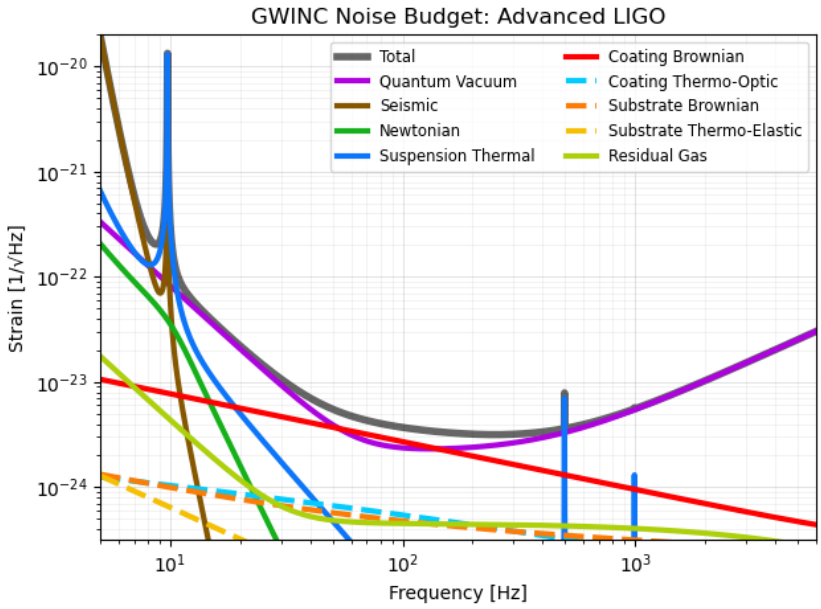

Figure 10 – Different noises of a ground-based interferometer.

Furthermore, the mHz region (below 10Hz) is potentially rich in gravitational wave (GW) sources, including supermassive black holes and first-order phase transitions in the early universe. To detect these, space-based interferometers are needed, as seismic and newtonian noise is absent in space. LISA consists of three spacecraft arranged in an equilateral triangle, 5 million km apart, orbiting the Sun. The triangle's center is about 50 million km behind the Earth along its orbit. The arm length is optimized to detect GWs in the 10 mHz range, with LISA sensitive to frequencies from 0.1 mHz to 0.1 Hz [42].

Each LISA spacecraft will carry two test masses, one for each arm, floating freely as shown in figure 11. The spacecraft uses a drag-free technique to keep centered on the test masses. The position of the masses is sensed, and the spacecraft adjusts its position using micro-thrusters, requiring extremely small thrusts—less than 100 μN. These tiny thrusts are generated by emitting fast ions in space, compensating for external influences

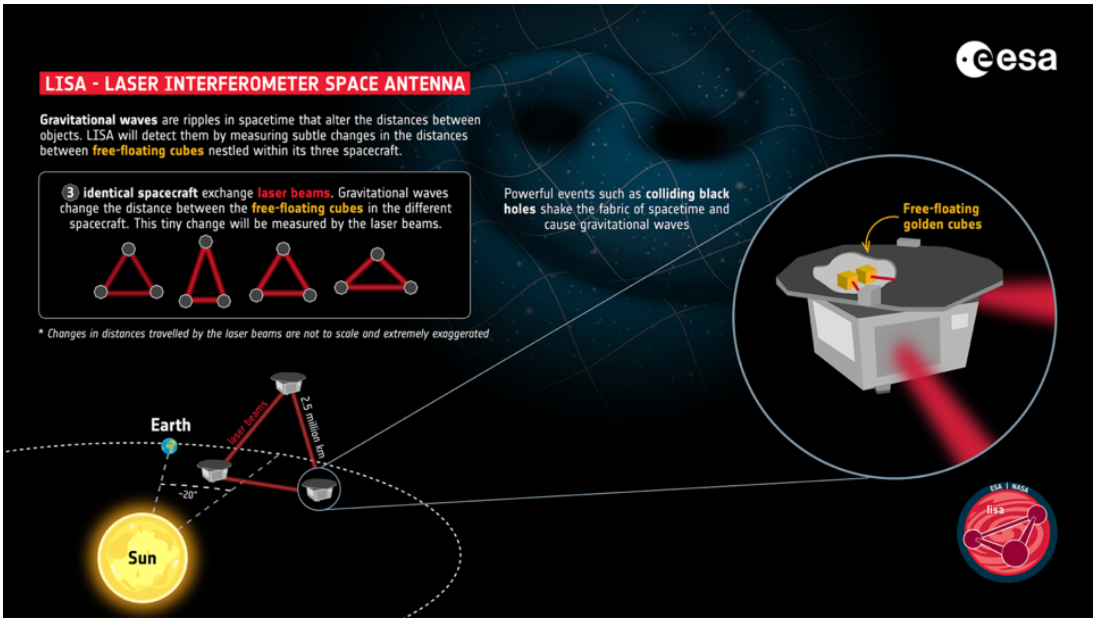

Figure 11 – LISA setup [42].

like solar winds and micro-meteorites. The LISA Pathfinder mission, an ESA initiative, demonstrated this drag-free control technique with the required precision [42].

The test masses exchange laser signals. Given the 5 million km distance, simple reflection is impractical due to power loss from diffraction, which spreads the beam over a 20 km radius. Instead, LISA employs a laser transponder system, where an incoming laser is sensed, and another laser, phase-locked to the first, sends back a return beam. Unlike a Michelson interferometer with equal arms, laser frequency fluctuations do not cancel out when taking the difference between arms. To address this, LISA employs time-delay interferometry, where the outputs of the two arms are recombined with a time delay that compensates for the arm length difference. This technique cancels laser frequency noise while preserving the signal from GWs in the mHz region.

LISA's sensitivity to gravitational waves in the frequency range of 10^{-4} Hz to 1 Hz makes it an ideal instrument for searching for signatures of early-universe phase transitions. If the electroweak phase transition is of first order and occurs at sufficiently high energy scale, $\mathcal{O}(1\text{ TeV})$, the resulting gravitational waves could fall within LISA's detectable range. A comparison of the sensitivities of various gravitational wave detectors is shown in Figure 12 [43].

According to the last section, the shape and peak of the power spectrum depend on the parameters of the phase transition. For our setup, one can plot the spectrum for several parameters of M and see where the spectrum falls within inside LISA‘s sensitivity, following [13], we implement equation 3.15 and 3.12 that give us the following spectrum , we see that the spectrum starts to become non-detectable at $M \approx 570\text{GeV}$. Therefore, a ϕ^6 model offers a straightforward approach to analyzing the behavior of detectable first-order

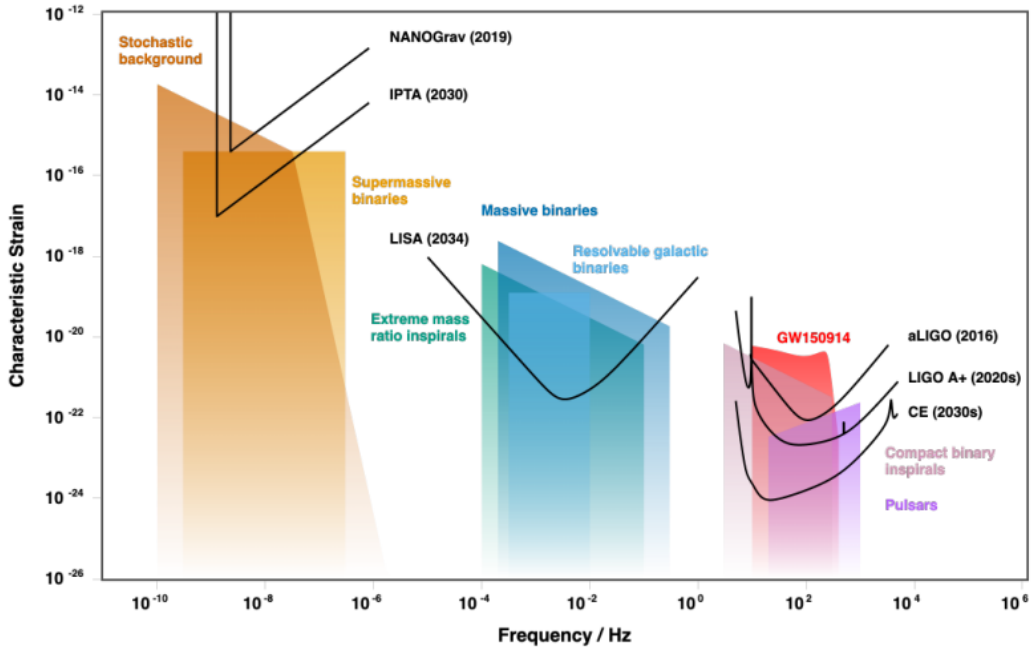

Figure 12 – Sensitivity plot from [43] showing the sensitivity curves of several gravitational wave detectors.

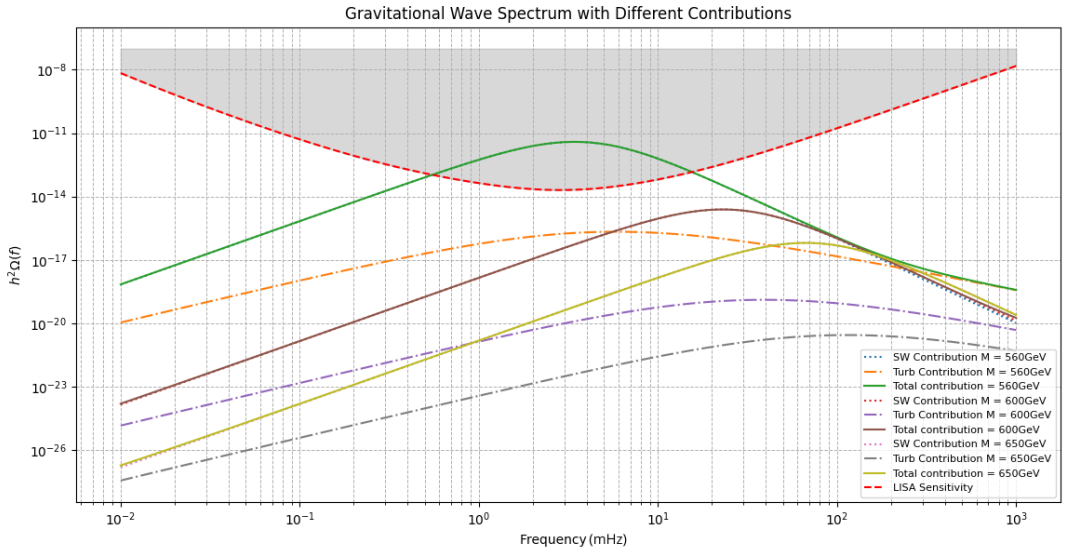

Figure 13 – Plot of the Gravitational Waves spectrum for several values of parameter M.

phase transitions.

4 Hydrodynamical effects

With the potential well-defined and the formulas established for computing the gravitational wave spectrum, we can now proceed to determine other important parameters that remain unknown. It's important to emphasize that our main focus here is to compute v_w. This chapter will provide an important nontrivial step to achieve that.

As the bubble propagates through the plasma, hydrodynamical effects are expected to arise. These effects can be analyzed using two complementary approaches, which should ultimately yield consistent results. The first approach relies on macroscopic physics, leveraging conservation laws such as energy and momentum conservation. The second approach, based on microscopic physics, will be the focus of the final sections.

For now, let us focus on the first approach that will give us important parameters and great insights on what is happening when the bubbles expands inside the plasma.

4.1 The energy-momentum tensor

The continuity of the total energy-momentum tensor across the bubble interface will be our guide to comprehend the profiles and effects that occurs with the bubble passage. The energy-momentum tensor of a scalar field is given by

$$T^{\phi}_{\mu\nu} = \partial_\mu\phi\partial_\nu\phi - g_{\mu\nu}\left(\frac{1}{2}\partial_\alpha\phi\partial^\alpha\phi - V_0(\phi)\right), \tag{4.1}$$

while that of a relativistic fluid in local equilibrium (perfect fluid) is

$$T^{\mathrm{pl}}_{\mu\nu} = (e+p)u_\mu u_\nu - g_{\mu\nu}p = w\,u_\mu u_\nu - g_{\mu\nu}p_T, \tag{4.2}$$

where u_μ is the four-velocity of the plasma, $w \equiv e + p_T$ is the enthalpy density, e is the energy density, and p_T is the pressure contribution due solely to the plasma particles.

We are interested in the energy-momentum far ahead of and behind the wall, where $\partial_\mu\phi = 0$, this illustration can be seen in figure 14.

Therefore, the total energy-momentum tensor is

$$T_{\mu\nu} = T^{\phi}_{\mu\nu} + T^{\mathrm{pl}}_{\mu\nu} = w\,u_\mu u_\nu - g_{\mu\nu}(p_T - V_0). \tag{4.3}$$

Note that $p_T - V_0 \equiv p$ acts as an effective total pressure, incorporating the free energy released by the scalar field during the phase transition. In fact, one can verify that $V_0 - p_T = V(T,\phi)$, which is the thermal effective potential of the scalar field, calculated in eq. (5.15) [44].

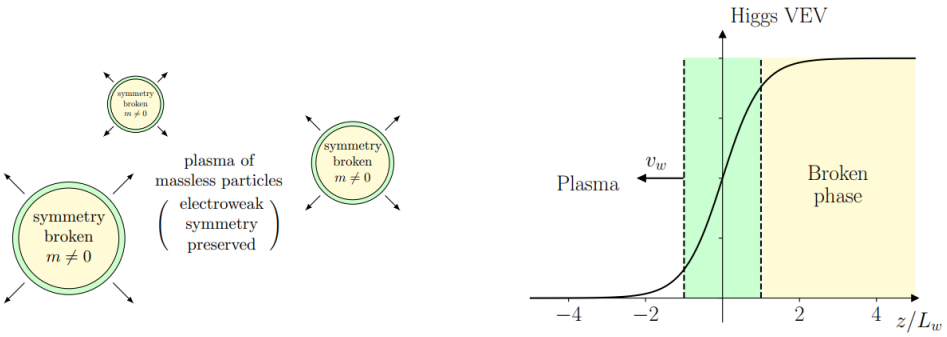

Figure 14 – Figure illustrating the bubble profile.

Focusing on the bubble wall frame with a terminal bubble wall velocity (constant velocity) leads to a time-independent energy-momentum tensor. Taking the z-component of eq. 4.3 and using the four-velocity $u^\mu = \gamma_z(1, v_z)$, the divergence of the energy momentum tensor gives the following equations:

$$\partial_z T^{zz} = 0 = \partial_z(\omega)\gamma_z^2 v_z^2 + \partial_z p, \quad \partial_z T^{z0} = \partial_z(\omega)\gamma_z^2 v_z. \tag{4.4}$$

Integrating these equations and denoting the phases in front and behind the wall by subscripts + (unbroken phase) and − (broken phase), we obtain the matching conditions:

$$w_+ v_+^2 \gamma_+^2 + p_+ = w_- v_-^2 \gamma_-^2 + p_- \quad \text{and} \quad w_+ v_+ \gamma_+^2 = w_- v_- \gamma_-^2. \tag{4.5}$$

Using thermodynamic relations,

$$w = p + \rho, \quad w = T\frac{\partial p}{\partial T}, \quad \text{and} \quad \rho = T\frac{\partial p}{\partial T} - p, \tag{4.6}$$

every term is well defined via our thermal potential.

4.2 The bag equation

For completeness, the plasma can be approximated, simplifying any numerical result for any type of potential. By using the thermal contribution in eq. 2.71, we can expand the free energy for bosons and fermions, truncating at the first term, which naturally leads to the so-called bag equation.

Expanding eq. 2.71 for $m \ll T$ [45], gives

$$\frac{V_1^\beta(\phi, T)}{T^4} = -\frac{\pi^2}{90} + \frac{1}{24}\left(\frac{m_i}{T}\right)^2 - \frac{1}{12\pi}\left(\frac{m_i}{T}\right)^3 - \frac{1}{32\pi^2}\left(\frac{m_i}{T}\right)^4 \ln\frac{m_i e^{\gamma_E - 3/4}}{4\pi T} + \cdots \tag{4.7}$$

for bosons, and

$$\frac{V_1^\beta(\phi, T)}{T^4} = -\frac{7}{8}\frac{\pi^2}{90} + \frac{1}{48}\left(\frac{m_i}{T}\right)^2 + \frac{1}{32\pi^2}\left(\frac{m_i}{T}\right)^4 \ln\frac{m_i e^{\gamma_E - 3/4}}{\pi T} + \cdots \tag{4.8}$$

for fermions. Then, it's easy to see that we can express $p = -\mathcal{F}$ satisfying the equation of state of a radiation gas, where the pressure has the form $p = aT^4/3$ and define the leading-order term

$$a = \frac{\pi^2}{30} \sum_i \left(N_b + \frac{7}{8} N_f \right), \tag{4.9}$$

which transforms the total free energy into

$$p = -\mathcal{F} = \frac{aT^4}{3} - V(\phi). \tag{4.10}$$

Using the thermodynamic relations 4.6,

$$w = aT^4 \quad \text{and} \quad \rho = aT^4 - p. \tag{4.11}$$

It is important to note that this expansion is only valid for $m_i \ll T$ and breaks down for particles with $m_i \sim T$ (including top quarks, W and Z bosons). However, this deviation is often minimal due to the dominance of light particle degrees of freedom (DoF) (remember, we are summing over all species and only few of then will not respect ($m_i << T$).

A relevant question now is whether this approximation is suitable for our model. To assess this, we can plot the thermal potential in eq. 2.71, computing the exact integral as well as the leading-order approximation from eq. 4.10 at the electroweak scale T 100 GeV. The respective masses of each Standard Model particle are used, as shown in 15.

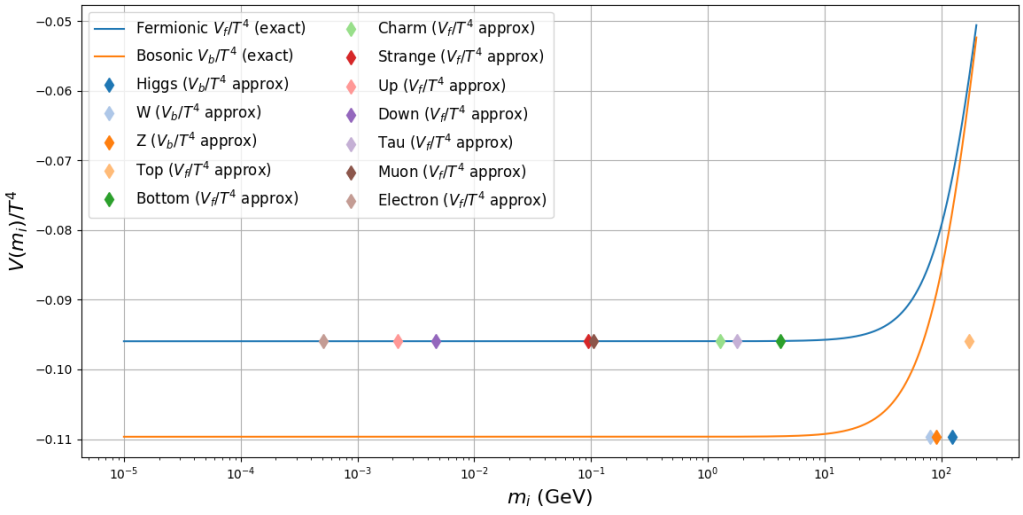

Figure 15 – Comparison between exact thermal contribution and Taylor expansion approximation.

As expected, the approximation converges for the light particles, and since most degrees of freedom are light particles, the sum over all Standard Model species yields a significant result. This approximation is advantageous for fast numerical computation of the thermal contribution.

4.3 Fluid equations

Another crucial hydrodynamic step is to determine the hydrodynamic variables in front of and behind the bubble wall. At a finite temperature, the bubble nucleates with the scalar profile given by the $O(3)$ bounce solution with spherical symmetry like 7, and the subsequent expansion is assumed to be spherical, making spherical coordinates convenient. Thus, the fluid velocity and other thermodynamic quantities depend only on the temporal and radial coordinates t and r, where r is the distance from the bubble center and t is the time since nucleation.

When the bubble reaches a steady expansion state long after nucleation, there is no characteristic distance scale for a steadily expanding bubble. Consequently, the fluid velocity and other thermodynamic quantities depend solely on the self-similarity coordinate $\xi = \frac{r}{t}$. In the planar wall case, the four-velocity of the plasma at a point ξ is $u^\mu = \gamma(1, v(\xi))$, where γ is the Lorentz factor associated with $v(\xi)$. We define a perpendicular direction $\overline{u}^\mu = \gamma(v(\xi), 1)$ such that $\overline{u}_\mu u^\mu = 0$, yielding

$$u^\mu \partial_\mu = -\frac{\gamma}{t}(\xi - v)\partial_\xi \quad \text{and} \quad \overline{u}^\mu \partial_\mu = \frac{\gamma}{t}(1 - v\xi)\partial_\xi. \tag{4.12}$$

Projecting the continuity equation along u_μ and the perpendicular direction $\overline{u}_\mu$, and using $u_\mu u^\mu = 1$ and $u_\nu \partial_\mu u^\nu = \frac{1}{2}\partial_\mu(u_\nu u^\nu) = 0$, we arrive at

$$\begin{aligned} \partial_z T^{00} = 0 \implies \frac{\partial_\xi e}{w} &= \frac{1}{\mu(\xi, v)}\left(2\frac{v}{\xi(1 - v\xi)} + \gamma^2 \partial_\xi v\right), \\ \partial_z T^{0z} = 0 \implies \frac{\partial_\xi p}{w} &= \gamma^2 \mu(\xi, v)\partial_\xi v, \end{aligned} \tag{4.13}$$

where we define

$$\mu(\xi, v) \equiv \frac{\xi - v}{1 - v\xi}. \tag{4.14}$$

We can rewrite $\partial_z T^{0z} = 0$ as an equation for the temperature profile using $w = T\frac{\partial \xi}{\partial T}\frac{\partial p}{\partial \xi}$ and then solving the differential integrating both sides to obtain

$$T(\xi) = T(\xi_0) \exp\left(\int_{v(\xi_0)}^{v(\xi)} \gamma^2 \mu(\xi(v), v)\, dv\right). \tag{4.15}$$

Now, using the sound speed $c_s^2 = \frac{\partial p}{\partial e} = \frac{\partial_\xi p}{\partial_\xi e}$, $\partial_z T^{00}$, and the same trick of the partial derivatives used to compute equation 4.15, we arrive at

$$\partial_v \xi = \frac{\xi}{2v}\frac{1 - v\xi}{1 - v^2}\left(\frac{\mu(\xi, v)^2}{c_s^2} - 1\right), \tag{4.16}$$

$$(\xi - v)\frac{\partial_\xi e}{w} = \frac{2v}{\xi} + [1 - \gamma^2 v(\xi - v)]\partial_\xi v, \tag{4.17}$$

$$(1 - v\xi)\frac{\partial_\xi p}{w} = \gamma^2(\xi - v)\partial_\xi v. \tag{4.18}$$

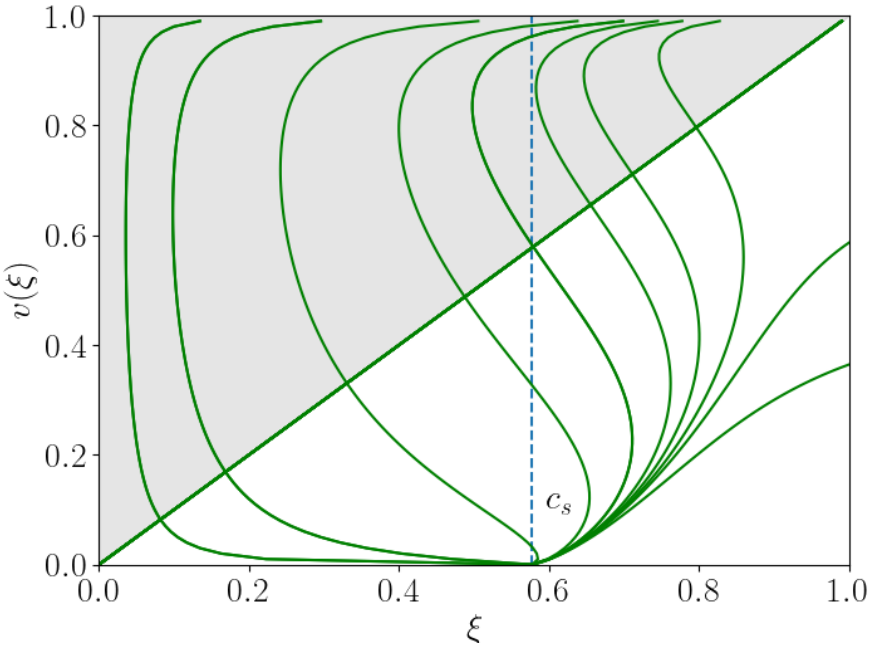

Figure 16 – General profiles of the fluid velocity $v(\xi)$ in the frame of the bubble center. There are no consistent solutions in the shaded regions.

This leads to the equation

$$2\frac{v}{\xi} = \gamma^2(1 - v\xi)\left(\frac{\mu(\xi, v)^2}{c_s^2} - 1\right)\partial_\xi v, \tag{4.19}$$

which can be solved for $\xi = \xi(v)$ and then substituted back into eq. (4.15) for the profile $T(\xi)$. Figure 16 shows different profiles of $v(\xi)$ for different initial conditions of ξ_0, v_0.

4.4 Classification of solutions and discontinuities

As demonstrated by the arguments above, equation (4.19) is central to hydrodynamic analysis. To better understand its solutions, we will rewrite the energy-momentum continuity across the bubble wall using the form 4.5. These equations can be combined to yield a relationship between the fluid velocities ahead of and behind the wall [46, 47]:

$$v_+ = \frac{1}{1+\alpha}\left(X_+ \pm \sqrt{X_-^2 + \alpha^2 + \frac{2}{3}\alpha}\right) \quad \text{with} \quad X_\pm \equiv \frac{3v_-^2 \pm 1}{6v_-}, \tag{4.20}$$

where

$$\alpha \equiv \frac{(w_+ - 3p_+) - (w_- - 3p_-)}{4\rho_{\text{rad}}} \tag{4.21}$$

defines the ratio of energy released by the transition relative to the energy contained in radiation in the plasma, $\rho_{\text{rad}} = \pi^2 T^4 \times 106.75/90$ [11, 48].

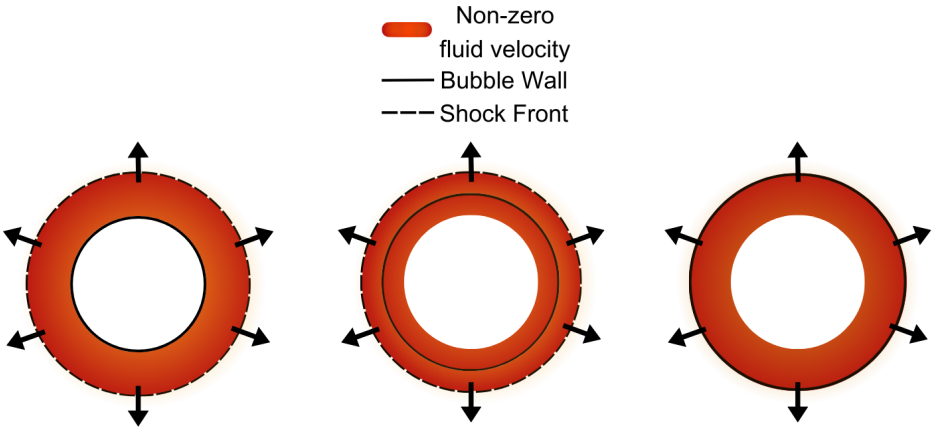

Figure 17 – Possible profiles of solutions from the hydrodynamic equation. From left to right: deflagrations, hybrids, and detonations.

We are now prepared to discuss the solutions of eq. (4.19). Depending on the initial conditions, consistent solutions exhibit distinct patterns of discontinuities, allowing for classification into three types, depicted in figures 17 and 18.

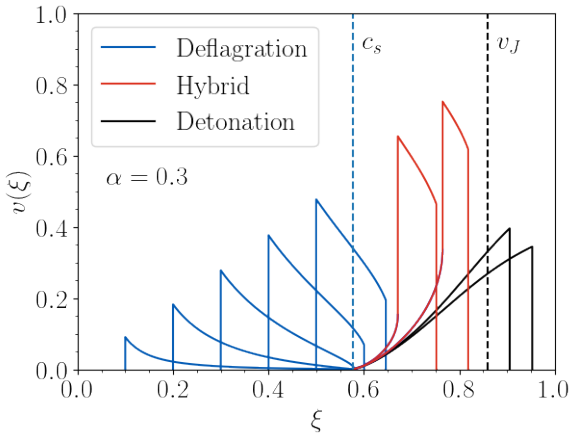

Figure 18 – Different velocity profiles $v(\xi)$ for deflagrations, hybrids, and detonations. Also shown are the speed of sound c_s and the Jouguet velocity v_J. The figure was produced with a fiducial value of $\alpha = 0.3$. This figure represents cases of the general profiles of figure 16

.

4.4.1 Detonations

One possible class of solutions is detonations, which occur when the wall velocity exceeds the so-called Jouguet velocity[1],

$$\xi_w > v_J = \frac{1}{\sqrt{3}} \frac{1 + \sqrt{2\alpha + 3\alpha^2}}{1 + \alpha}. \tag{4.22}$$

[1] Obtained from the Chapman-Jouguet condition, which gives $v_- = c_s$ for detonations [46, 48, 49].

In this scenario, the wall encounters the plasma while it is still at rest. Thus, the plasma immediately ahead of the bubble wall remains unaffected, with a temperature $T_+ = T_n$.

4.4.2 Deflagrations

Another solution class is deflagrations, where the wall propagates at subsonic velocities, $\xi_w \equiv v_w < c_s$, accompanied by a shock wave that precedes the bubble wall, heating the plasma. This is illustrated in figure 19. The shock front velocity $\xi_{\rm sh}$ can be determined as follows. In the plasma frame (also known as the "bubble center frame" in the literature, where the plasma is at rest at infinity), the plasma is stationary ahead of the shock and moves with velocity $v(\xi_{\rm sh})$ immediately behind it. Transforming to the shock frame using Lorentz velocity addition, eq. (4.14), the plasma moves with velocity $-\xi_{\rm sh}$ ahead of the shock and with $-\mu(\xi_{\rm sh}, v(\xi_{\rm sh}))$ behind it. Given that the plasma remains in the broken phase on both sides of the shock, eq. (4.5) yields the condition [46, 48, 50]:

$$\xi_{\rm sh}\mu(\xi_{\rm sh}, v(\xi_{\rm sh})) = \frac{1}{3} \qquad \text{and} \qquad \frac{\xi_{\rm sh}}{\mu(\xi_{\rm sh}, v(\xi_{\rm sh}))} = \frac{3T_{\rm sh}^4 + T_n^4}{3T_n^4 + T_{\rm sh}^4}. \tag{4.23}$$

Rewriting the first equation gives

$$\xi_{\rm sh} = \frac{v(\xi_{\rm sh})}{3} + \sqrt{\frac{v(\xi_{\rm sh})^2}{9} + \frac{1}{3}}. \tag{4.24}$$

The shock front position can thus be found by solving eq. (4.19) for $v(\xi)$ and identifying where $v(\xi)$ satisfies eq. (4.24).

The second condition in eq. (4.23) can then be used to establish the temperature jump across the shock front:

$$\frac{T_n}{T_{\rm sh}} = \left(\frac{3(1-\xi_{\rm sh}^2)}{9\xi_{\rm sh}^2 - 1}\right)^{1/4}. \tag{4.25}$$

From eqs. (4.15) and (4.25), we have

$$\frac{T_n}{T_+} = \frac{T_n}{T_{\rm sh}} \cdot \frac{T_{\rm sh}}{T_+} = \left(\frac{3(1-\xi_{\rm sh}^2)}{9\xi_{\rm sh}^2 - 1}\right)^{1/4} \exp\left(\int_{v(\xi_w)}^{v(\xi_{\rm sh})} \gamma^2 \mu(\xi(v), v)\, dv\right), \tag{4.26}$$

where $\xi(v)$ is obtained by solving eq. (4.19). For deflagrations, the plasma is at rest behind the wall (in the plasma frame), so in the bubble frame, $v_- = -\xi_w$. Given T_+ and v_-, we can solve the continuity equations (4.5) to find T_- and v_+ (the fluid velocity in front of the wall in the wall frame). Using v_+, the fluid velocity ahead of the wall in the plasma frame is computed as $v(\xi_w) = \mu(\xi_w, v_+)$, allowing for the initial conditions to solve eq. (4.19) and find $v(\xi_{\rm sh})$. The integration in eq. (4.26) yields $T_n(T_+, v_w)$. For a fixed ξ_w, this process iterates until $T_n(T_+, v_w)$ matches the nucleation temperature calculated in the previous section, determining T_+.

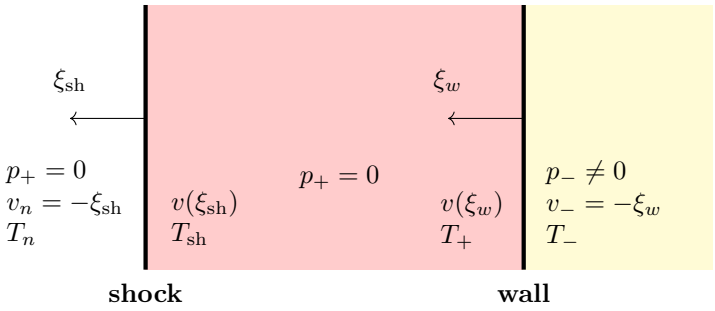

Figure 19 – Depiction of the wall and shock fronts. Behind the wall (yellow region to the right), the plasma is in the broken phase ($p_- \neq 0$) and at rest, so the plasma velocity in the bubble frame is $v_- = -\xi_w$. Ahead of the shock front (white region to the left), the plasma is also at rest, giving a velocity of $-\xi_{\rm sh}$ in the shock frame. The temperature T_+ immediately ahead of the wall is found by calculating the temperature jump from T_n to $T_{\rm sh}$ across the shock front, then evolving to the wall along the shock wave (red region in between) using eq. (4.15).

4.4.3 Hybrids

Another kind of solution is called hybrids, which occurs for supersonic walls ($\xi_w > c_s$). Unlike Jouguet detonations, hybrids involve a shock front ahead of the wall, as well as a rarefaction wave behind it. The method for computing T_+ in this case is similar to the one used for deflagrations described above. However, the plasma is no longer at rest behind the wall; instead, it moves at the speed of sound (in the wall frame) [46, 51]. Thus, one must set $v_- = c_s$ in the continuity equations.

4.5 Behavior of T_+, T_-, v_+, v_-

Now that we have the tools to compute T_+, T_-, v_+, v_- for a given v_w one can plot a graph of v_+ as a function of ξ_w to illustrate the dependence described in equation 4.19. This can be done for a low value of M (e.g., $M = 600$ GeV) and for a high value ($M = 820$ GeV), showing that the difference between v_+ and v_- is highly dependent on the strength of the transition. Higher values of M lead to closer values of v_+ and v_-, as one would expect in the standard model limit where $M \to \infty$. This behavior is clear in figure 20.

With these plots, one can see the propositions made in this section. In the deflagration case, the plasma is at rest right behind the wall, so that the wall velocity is now $v_- = v_w$, and the relation $v_+ < v_-$ is valid due to the shock front created. In contrast, in detonations, the phase transition wall moves at supersonic speed hitting fluid that is at rest in front of the wall. In the wall frame, the symmetric-phase fluid moves into the wall at $v_+ = v_w$ and entering the broken phase behind the wall where it slows down so that $v < v_+$ (e.g. the fluid gains mass). We can also see in the hybrids region that we have

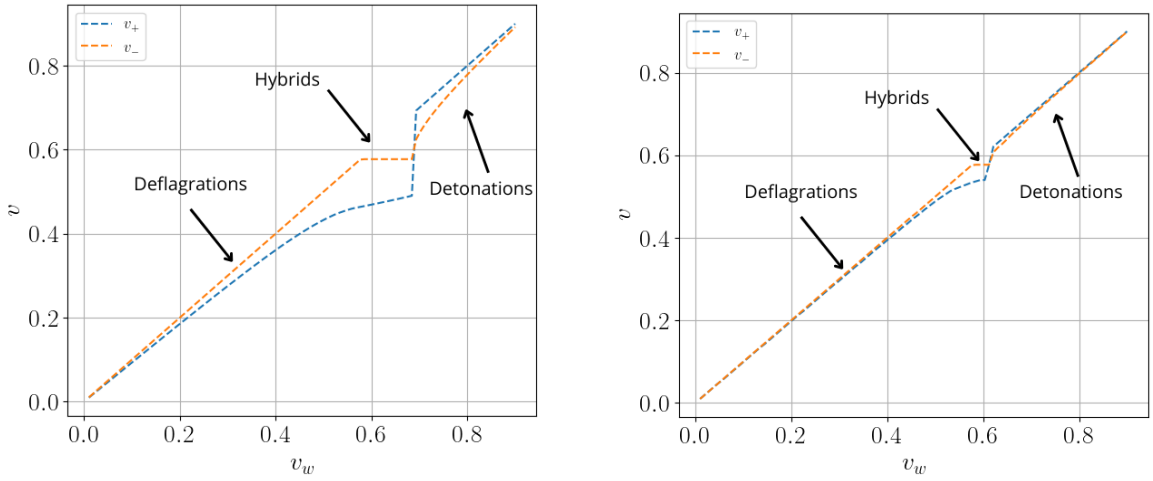

Figure 20 – Plots showing the dependence of v_+ and v_- with the parameter v_w as an input. The left picture shows the plot for $M = 600$GeV and the right one for $M = 820$GeV. The velocities until $v_w = 1/\sqrt{3}$ refers to deflagrations, from c_s to v_J, Hybrids, and after the descontinuity, detonations.

.

$v_- = c_s$ while v_+ still gets constrained by the shock front.

We can also plot the dependence of T_+ and T_- as functions of ξ_w seen in figure 21: Again, the difference between T_+ and T_- decreases as the transition strength weakens.

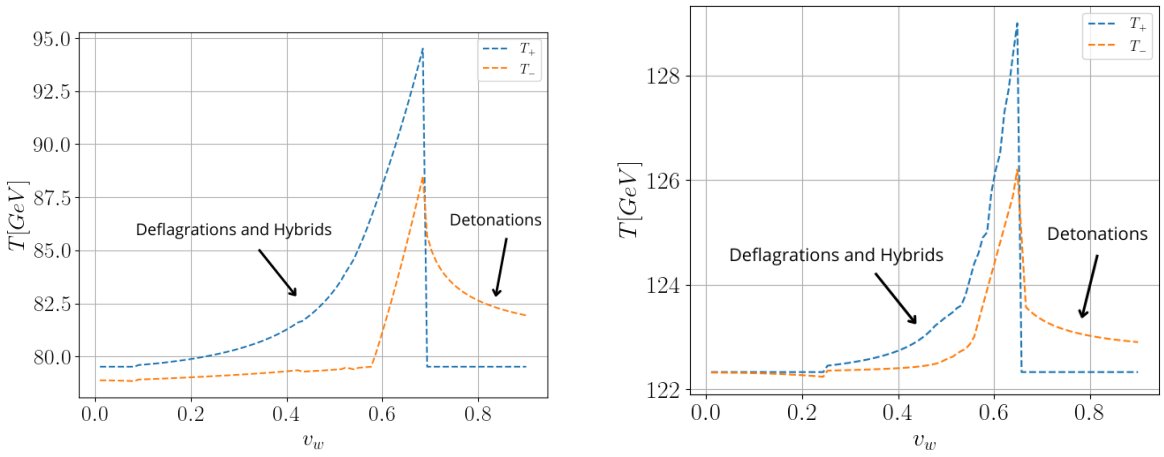

Figure 21 – Plots showing the dependence of T_+ and T_- with the parameter v_w as an input. The left picture shows the plot for $M = 600$ GeV and the right one for $M = 820$ GeV.

Additionally, this plot highlights a key feature of the behavior of T_+ and T_-: a discontinuity appears at v_J. This arises because, in deflagrations and hybrid transitions, the temperature T_+ does not match the ambient plasma temperature outside the shock, T_n. This discrepancy results from changes in thermodynamic quantities both ahead of the wall and at the shock

front, which intuitively leads to distinct conditions in the bubble's front as hybrids transition to detonations. Note that, in detonations, the absence of a shock front means information has not propagated to the bubble's front. Thus, T_+ converges to T_n immediately after reaching v_J. This process also causes a friction discontinuity ahead of the bubble, which will be further discussed in the next section.

5 Non-equilibrium effects

Now that we have developed methods to understand the macroscopic behavior of the solutions for bubble propagation, let us delve into the microphysics of the problem. In this section, we will explore how to describe the system in a nonequilibrium framework, with the understanding that, in the appropriate asymptotic limits, these microscopic descriptions should converge to the macroscopic properties previously derived. To tackle this complex approach to nonequilibrium physics, we will begin by examining the renowned Kadanoff-Baym equations.

5.1 The Boltzmann equation

The dynamics of particles in the plasma are described by the Kadanoff-Baym equations, a set of integro-differential equations used in nonequilibrium quantum field theory to explain the time evolution of Green's functions (or correlation functions) in systems out of equilibrium [52].

In the context of the Kadanoff-Baym formalism, certain two-point functions encode the dynamics of the system. In particular, the Wightman function $G^<$ encodes the particle distribution functions,

$$G^<(p,x) = 2\pi f(\vec{p},x)\delta(p^2 - m^2). \tag{5.1}$$

It can also be shown that this function satisfies the typical condition of a Green's function. This function describes the distribution of particles and the correlations of the field in momentum space. It can be shown that [53], to leading order in a gradient expansion, when the wall width is taken to be much larger than typical particle momenta in the plasma, i.e. $L_w \gg 1/T$, the dynamical equation of this function is given by the Boltzmann equation by the kinetic and collision terms inside Kadanoff-Baym equation:

$$\left(p^\mu \partial_\mu + \frac{1}{2}\partial_\mu m^2 \partial_{p^\mu}\right) G^<(p,x) = \text{coll.} \tag{5.2}$$

This equation describes how the quantum field evolves out of equilibrium, including both free propagation (via the Louville term) and the interactions (represented by the collision term). The collision term (coll) describes how the particle distribution changes due to interactions, such as,

- Particle creation or annihilation.
- Scattering processes (e.g., top-top scattering in a plasma).

In the case of a field undergoing dynamics driven by interactions, the evolution described by the Boltzmann equation equations considers both quantum fluctuations (through the Green's functions) and statistical effects (through the collision integral). The equation 5.1is the constraint equation, which encodes the fact that the Wightman function $G^<$ can be expressed in terms of the particle distribution function $f(\mathbf{p}, x)$, this relationship allows us to derive various physical quantities (such as currents or observables) from the system's statistical properties. The interesting aspect of equation (5.2) is that it leads to the Boltzmann equation in a 3-dimensional space. It's easy to see that the term $p^\mu \partial_\mu$, with $\gamma = 1$, leads to:

$$p^\mu \partial_\mu = m(\partial_t + \vec{v} \cdot \nabla), \tag{5.3}$$

which is the usual kinetic term in the Boltzmann equation. The term involving the derivative of the momentum is the usual force term in 4-dimensional space, and the collision term takes into account the interactions involved in the thermodynamical content of the plasma. It also relates to the quantum field theory of the problem (through interactions), which we will discuss in detail later in the collision terms.

Let's then, move to create an approach that allows us to deal with such complexity and solve this complex equation.

5.2 The friction term

We discussed that we are interested in the velocity of this wall once the growing bubble reaches a steady expansion regime. To compute this speed, one needs the equation of motion for the Higgs in the plasma. One achieves this by using the energy-momentum conservation of all particles in the plasma and the Higgs background:

$$\partial_\mu T^{\text{total}}_{\mu\nu} = \partial^\mu \left(\sum_n T^{\text{plasma}}_{n,\mu\nu} + T^{\phi}_{\mu\nu} \right) = 0, \tag{5.4}$$

n being the species inside the plasma. The energy-momentum tensor of the plasma for each species n can be expressed as the usual formula:

$$T^{\text{plasma}}_{n,\mu\nu} = \int \frac{d^4p}{(2\pi)^4} p_\mu p_\nu G^<_n(p, x) = \int \frac{d^3p}{(2\pi)^3} \frac{p_\mu p_\nu}{E_n} f_n(\mathbf{p}, x), \tag{5.5}$$

where $p^0 = E_n$. Next, we compute the divergence of the energy-momentum tensor $T^{\text{plasma}}_{n,\mu\nu}$. To do this, we apply the derivative ∂_μ to the energy-momentum tensor:

$$\partial^\mu T^{\text{plasma}}_{n,\mu\nu} = \partial^\mu \int \frac{d^3p}{(2\pi)^3} \frac{p_\mu p_\nu}{E_n} f_n(\mathbf{p}, x) \tag{5.6}$$

Taking the divergence of the tensor of the plasma and subtracting with the coll term of equation 5.2,

$$\partial^\mu T^{\text{plasma}}_{n,\mu\nu} - \text{coll}_n = -\frac{1}{2} \partial_\mu m_n^2 \int \frac{d^4p}{(2\pi)^4} p^\nu \partial_{p^\mu} G^<_n(p, x),$$

This equation describe how the collision terms and the passage of the bubble alter the distribution of particles in the plasma, and therefore the distribution of energy-momentum among the species. Integrating by parts leads to:

$$\begin{aligned} &-\frac{1}{2}\partial_\mu m_n^2 \int \frac{d^4p}{(2\pi)^4} p^\nu \partial_{p^\mu} G_n^<(p,x) = \frac{1}{2}\partial_\nu m_n^2 \int \frac{d^4p}{(2\pi)^4} G_n^<(p,x) \\ &= \frac{1}{2}\partial_\nu m_n^2 \int \frac{d^3p}{(2\pi)^3} \frac{1}{E_n} f_n(\mathbf{p},x), \end{aligned} \tag{5.7}$$

where E_n denotes the energy of species n. On the other hand, the energy-momentum tensor of the classical field background is given by:

$$T^\phi_{\mu\nu} = \partial_\mu\phi\partial_\nu\phi - g_{\mu\nu}\left(\frac{1}{2}\partial_\rho\phi\partial^\rho\phi - V(\phi)\right). \tag{5.8}$$

The divergence of this energy-momentum tensor is:

$$\partial_\mu T^\phi_{\mu\nu} = \partial_\nu\phi\left(\Box\phi + \frac{dV}{d\phi}\right). \tag{5.9}$$

Finally, by plugging Eqs. (5.7) and (5.9) into Eq.(5.4), one obtains the Higgs equation of motion:

$$\Box\phi + \frac{dV}{d\phi} + \sum_n \frac{dm_n^2}{d\phi}\int \frac{d^3p}{(2\pi)^3}\frac{1}{2E_n} f_n(\mathbf{p},x) = 0. \tag{5.10}$$

Note that the collision terms are absent in this equation; they cancel out when the sum over all species is performed. Here, $f_i(p,x)$ is the distribution function of particle i, and g_i represents its number of degrees of freedom.

As we are dealing with a non-equilibrium case, one can decompose $f_i(p,x)$ into an equilibrium and a non-equilibrium part:

$$f_i(p,x) = f_i^{eq}(p) + \delta f_i(p,x), \quad \text{with} \quad f_i^{eq}(p) = \frac{1}{e^{\beta p^\mu u_\mu - \delta_p - \delta_{\rm bg}} \mp 1}, \tag{5.11}$$

where u_μ is the plasma four-velocity, $\beta \equiv 1/T$ is the inverse temperature, and the sign $\mp$ distinguishes bosons and fermions, respectively. The fluctuations δ can be expanded in powers of momentum [22]:

$$\delta(x,p) = w^{(0)}(x) + p^\mu w^{(1)}_\mu(x) + p^\mu p^\nu w^{(2)}_{\mu\nu}(x) + \dots \tag{5.12}$$

It is worthwhile emphasizing that, up to this point, this approach is fully generic: any fluctuation δf can be expressed in the form (5.12) for some function $\delta(x,p)$, and any such function can be expanded in powers of momenta, which is essentially an expansion in the 4D generalized version of spherical harmonics [54]. Since these generalized spherical harmonics form a complete set in the functional space, this expansion is expected to converge for any reasonably well-behaved function δf.

However, we will make one further approximation, assuming that the fluctuations $w^{(i)}$ are sufficiently small to linearize the following expression:

$$\delta f = \delta(x,p)\,(-f'^{\mathrm{eq}})\,, \tag{5.13}$$

where f'^{eq} is the derivative of the equilibrium distribution function given in Eq. (5.11) with respect to $p^\mu u_\mu$.

Going back to the EOM, in the plasma rest frame, $p^\mu u_\mu = E = \sqrt{\mathbf{p}^2 + m^2}$, so

$$\frac{1}{2}\frac{\partial m_i^2}{\partial \phi}\int \frac{d^3p}{(2\pi)^3 E_i} f_i^{eq}(p) = \pm T \frac{\partial}{\partial \phi}\int \frac{d^3p}{(2\pi)^3}\log\left(1 \mp e^{-\beta\sqrt{\mathbf{p}^2+m^2}}\right). \tag{5.14}$$

This term can be absorbed into V_0 to yield the effective thermal potential:

$$V(T,\phi) \equiv V_0 + \sum_i (\pm g_i)\frac{T^4}{2\pi^2}\int_0^\infty dp\, p^2\, \log\left(1 \mp e^{-\beta\sqrt{p^2+(m/T)^2}}\right), \tag{5.15}$$

where the upper sign corresponds to bosons and the lower one to fermions. The Klein-Gordon equation for the scalar field immersed in the plasma can now be written as:

$$\Box\phi\,\partial_\nu\phi + \frac{\partial V(T,\phi)}{\partial\phi}\partial_\nu\phi + \sum_i \frac{g_i}{2}\frac{\partial m_i^2}{\partial\phi}\partial_\nu\phi\int\frac{d^3p}{(2\pi)^3 E_i}\delta f_i(p,x) = 0. \tag{5.16}$$

Notice that the potential in equation 5.10 represents only the non-thermal contribution and now our Klein-Gordon equation also include the thermal contributions, but the third term is still unknown. What we can do here is insert an Ansatz into these fluctuations, considering a small variation in the temperature, chemical potential, and the velocity of the fluid relative to the background properties.

5.3 Recalling the Boltzmann equation

Now that the nonequilibrium distribution setup is established, we can tackle the Boltzmann equation, one of our most challenging tasks. The Boltzmann equation 5.2 can be expanded similarly to Eq. (5.11) to understand the physics of each contribution. This expansion leads to:

$$(p^\mu\partial_\mu + \frac{1}{2}\partial_\mu m^2\partial_{p_\mu})f_{\mathrm{eq}} + (p^\mu\partial_\mu + \frac{1}{2}\partial_\mu m^2\partial_{p_\mu})\delta f = \mathrm{coll.} \tag{5.17}$$

On the left-hand side (LHS) of this equation, we can identify and discuss two different terms. First, the source term:

$$\mathrm{Source} = (p^\mu\partial_\mu + \frac{1}{2}\partial_\mu m^2\partial_{p_\mu})f_{\mathrm{eq}}. \tag{5.18}$$

This term acts as a *driving force* arising due to changes in the equilibrium distribution f_{eq}. Physically, f_{eq} evolves because of variations in system parameters, such as the mass

m, temperature T, or chemical potential μ. This term is called the *source term* because it introduces deviations from equilibrium due to external changes in the system (e.g., a z-dependence mass or a temperature gradient[1]).

Next, we identify the "kinetic term":

$$\text{Kinetic} = \left(p^\mu \partial_\mu + \frac{1}{2}\partial_\mu m^2 \partial_{p_\mu}\right) \delta f.$$

This term describes how the deviation from equilibrium (δf) evolves due to particle motion (kinematics). Physically, it captures the dynamics of how deviations from equilibrium evolve due to particle motion independent of the equilibrium state.

The right-hand side (RHS) of Eq. (5.2) represents the collision terms, which are limited to $2 \to 2$ processes, each characterized by an amplitude $\mathcal{M}_{pk\to p'k'}$. The collision term is expressed as:

$$\text{coll} = \mathcal{C}[f_p] = \frac{1}{2}\sum_{\text{processes}} \int \frac{d^3k\, d^3p'\, d^3k'}{(2\pi)^9 2E_k\, 2E_{p'}\, 2E_{k'}} |\mathcal{M}_{pk\to p'k'}|^2 (2\pi)^4 \delta^4(p + k - p' - k') \mathcal{P}_{pk\to p'k'}, \tag{5.19}$$

where

$$\mathcal{P}_{pk\to p'k'} \equiv f_p f_k (1 \pm f_{p'})(1 \pm f_{k'}) - f_{p'} f_{k'} (1 \pm f_p)(1 \pm f_k) \tag{5.20}$$

is the population factor, which accounts for how the number density of reactants and products in the plasma influences the reaction rate. The first term in $\mathcal{P}$, proportional to $f_p f_k$, means that a process $pk \to p'k'$ is more efficient when more reactants are present in the plasma. Likewise, the number density of outgoing particles also influences the overall rate, taken into account by the factors $(1 \pm f)$, which correspond to stimulated emission (for bosons, the "+" sign) or Pauli blocking (for fermions, the "-" sign). The second term in $\mathcal{P}$, with an overall negative sign, accounts for the reverse process $p'k' \to pk$.

Now, to solve the Boltzmann equation for the fluctuations δf_i, one first needs to find an efficient way to compute the collision terms. To illustrate the procedure, let us first limit ourselves to first-order terms in the momentum expansion, so that the fluctuations in Eq. 5.12 are parametrized as:

$$\delta = \delta\mu + p^\mu \left(\delta u_\mu - \frac{u_\mu \delta T}{T}\right). \tag{5.21}$$

It is important to emphasize that this procedure of considering only first-order terms in momentum is a tool to facilitate the calculation of momentum elements from the Boltzmann equation. The total approach, however, can be extended to any order in the momentum expansion, as seen in Eq. 5.12. In this context, $\delta\mu$ represents the particle's

[1] In our case, the z-dependence of the mass.

chemical potential, $\delta T/T$ tracks fluctuations in the fluid temperature, and δu_μ (which satisfies $u^\mu \delta u_\mu = 0$) represents the velocity fluctuations.

Furthermore, we assume that the bubble has expanded sufficiently so that the effects of the wall curvature are negligible, and the problem becomes one-dimensional, similarly to what we also assumed in the hydrodynamical considerations. In the rest frame of the bubble wall, with the z-axis orthogonal to the wall and oriented towards the broken phase, we have $u^\mu = \gamma_w(1, v_w)$, $\delta u^\mu \equiv \delta v\, \bar{u}_\mu = \delta v \gamma_w(v_w, 1)$, and $m^2(x) \to m^2(z)$.

To proceed, we take three moments of the Boltzmann equation, multiplying it by 1, $p^\mu u_\mu$, and $p^\mu \bar{u}_\mu$ (where $\bar{u}_\mu$ is the four-velocity orthogonal to u_μ), and integrating over p. This is a common procedure used in Boltzmann equation in textbooks of Comoslogy [55]to take out information of this complex equation.

Let us first apply this method in a generic form, and then explicitly show the first-order perturbation in Eq. 5.28 to understand the mechanism of taking moments from the Boltzmann equation.

5.4 Taking moments

As discussed in the previous section, the strategy to solve the Boltzmann equation involves taking moments of the equation. To do this, first divides the Boltzmann equation by the energy, leading to the following form:

$$p^\mu \frac{\partial_\mu \delta f}{E_p} = \frac{C[f]}{E_p} + \frac{S}{E_p}. \tag{5.22}$$

One can multiply this equation by powers of momentum and energy, as in $(p^\mu u_\mu)^a$ and $(p^\mu \bar{u}_\mu)^b$, which includes finer details of the distribution function. Due to this form of taking moments, we will see that we will often encounter terms of the form,

$$\int \frac{d^3p}{E} \left(p^\mu u_\mu\right)^m \left(p^\nu \bar{u}_\nu\right)^n \left(-f'_{\rm eq}\right) = 4\pi T^{m+n+2} \begin{cases} \frac{c_{m+n+1}}{n+1}, & n \text{ even}, \\ 0, & n \text{ odd}. \end{cases} \tag{5.23}$$

This integral is constant in the massless case, and for $n \geq 2$, we have:

$$\begin{aligned} c_n^b &\equiv \frac{1}{T^{n+1}} \int dp\, p^n f_p^{\rm BE} \left(1 + f_p^{\rm BE}\right) = n! \zeta_n, \\ c_n^f &\equiv \frac{1}{T^{n+1}} \int dp\, p^n f_p^{\rm FD} \left(1 - f_p^{\rm FD}\right) = \left(1 - \frac{1}{2^{n-1}}\right) n! \zeta_n, \end{aligned} \tag{5.24}$$

with $f^{\rm BE}$ and $f^{\rm FD}$ denoting the Bose-Einstein and Fermi-Dirac distribution functions, respectively, for the collision terms associated with annihilation it will also be convenient to define

$$\tilde{c}_{n+1} \equiv \frac{1}{T^{n+1}} \int dp\, p^n f_p^{\rm FD} \left(1 + f_p^{\rm BE}\right) = \left(1 - \frac{1}{2^{n+1}}\right) n! \zeta_{n+1}. \tag{5.25}$$

These integrals can be easily solved by choosing a reference frame where $p^\mu u_\mu = E$.

Now, with this machinery of definitions, one can exploit the first-order momentum terms in the Boltzmann equation to understand all three components before expressing them in the generic form that will be implemented in our code.

5.4.1 Kinetic terms

Analyzing the first-order perturbations, we can consider three types of momentum from the Boltzmann equations: (1, $p^\mu u_\mu$ and $p^\mu \bar{u}_\mu$).The shape of the kinetic terms are:

$$\gamma \int \frac{d^3p}{E} p^\mu \partial_\mu \delta f. \tag{5.26}$$

To handle these terms, we define the coordinate $\xi = x^\mu v_\mu$, where $v_\mu = \gamma_w(v_w u_\mu - \bar{u}_\mu)$, essentially decomposing in the velocity direction and its perpendicular four-velocity direction. Recalling equation 5.28,

$$\delta_p = \delta\mu + p^\mu(\delta u_\mu - u_\mu \delta T/T), \tag{5.27}$$

we see that equation 5.26 becomes

$$\gamma \int \frac{d^3p}{E} p^\mu (v_w u_\mu + \bar{u}_\mu)\partial_\xi \delta f = \gamma \int \frac{\delta d^3p}{E} p^\mu (v_w u_\mu + \bar{u}_\mu)\partial_\xi [\delta_p(-f'_{eq})] \tag{5.28}$$

The derivative inside the fluctuation applies only to δ_p. The derivative $\partial_\xi(-f'_{eq})$ is considered a second-order term in our linearization of equation 5.13 (our taylor expansion is truncated until first-order) and can be neglected. Now, let's proceed with the moments.

- First moment

The first moment of the kinetic terms is:

$$\gamma \int \frac{d^3p}{E} p^\mu (v_w u_\mu + \bar{u}_\mu)\partial_\xi [\delta_p(-f'_{eq})] \tag{5.29}$$

Substituting equation 5.28 into the first momentum, we analyze each term of the fluctuations. For the μ term, we obtain:

$$\gamma \int \frac{d^3p}{E} p^\mu (v_w u_\mu + \bar{u}_\mu)\partial_\xi \delta\mu(-f'_{eq}) = \gamma \int \frac{d^3p}{E} p^\mu u_\mu (v_w)\partial_\xi(\mu)(-f') \tag{5.30}$$

$$+ \gamma \int \frac{d^3p}{E} p^\mu \bar{u}_\mu \partial_\xi(\mu)(-f') = 4\pi T^3 v_w c_2 \partial_\xi(\mu) \tag{5.31}$$

Here, we directly applied equation 5.23. This equation will be useful for any order in our Ansatz. For the velocity fluctuation, we have:

$$\int \frac{d^3p}{E} p^\mu \partial_\mu p^\mu \bar{u}_\mu (\delta v/T)(f') = \gamma \int \frac{d^3p}{E} p^\mu u_\mu p^\mu \bar{u}_\mu (v_w)\partial_\xi(\delta v/T)(-f') \tag{5.32}$$

$$+ \gamma \int \frac{d^3p}{E} (p^\mu \bar{u}_\mu)^2 \partial_\xi(\delta v/T)(-f') = 4\pi T^3 (c_3/3)\partial_\xi(\delta v) \tag{5.33}$$

In this case, the first term has an odd n and the second has an even n, leading to a $c_3/3$ term.

For the third perturbation $\delta T/T$, we obtain:

$$\int \frac{d^3p}{E} p^\mu \partial_\mu p^\mu u_\mu (\delta T/T^2)(-f') = \gamma v_w \int \frac{d^3p}{E} p^\mu u_\mu p^\mu u_\mu \partial_\xi (\delta T/T^2)(-f') \tag{5.34}$$

$$+\gamma \int \frac{d^3p}{E} (p^\mu \bar{u}_\mu)^2 p^\mu \bar{u}_\mu \partial_\xi (\delta T/T^2)(-f') = 4\pi v_w T^3 (c_3) \partial_\xi (\delta T/T). \tag{5.35}$$

Now that we understand the machinery for using equation 5.23, we can easily compute the other two moments. For $p^\mu u_\mu$, we get terms like:

$$\int \frac{d^3p}{E} p^\mu p^\mu u_\mu \partial_\mu (\delta\mu/T)(-f'_{eq}) = 4\pi T^4 (c_3) \partial_\xi (\delta\mu), \tag{5.36}$$

$$\int \frac{d^3p}{E} p^\mu p^\mu u_\mu \partial_\mu p^\mu \bar{u}_\mu (\delta v/T)(-f'_{eq}) = 4\pi T^4 (c_4/3) \partial_\xi (\delta v), \tag{5.37}$$

$$\int \frac{d^3p}{E} p^\mu p^\mu u_\mu \partial_\mu p^\mu u_\mu (\delta T/T)(-f'_{eq}) = 4\pi T^4 (c_4) \partial_\xi (\delta T). \tag{5.38}$$

For $p^\mu \bar{u}_\mu$, we obtain:

$$\int \frac{d^3p}{E} p^\mu p^\mu \bar{u}_\mu \partial_\mu (\delta\mu/T)(-f'_{eq}) = 4\pi T^4 (c_3/3) \partial_\xi (\delta\mu), \tag{5.39}$$

$$\int \frac{d^3p}{E} p^\mu p^\mu \bar{u}_\mu p^\mu \bar{u}_\mu \partial_\mu (-f'_{eq}) \left(\frac{\delta v}{T}\right) = 4\pi T^4 (c_4) \partial_\xi (\delta v), \tag{5.40}$$

$$\int \frac{d^3p}{E} p^\mu p^\mu \bar{u}_\mu p^\mu u_\mu \partial_\mu \left(\frac{\delta T}{T^2}\right) (-f'_{eq}) = 4\pi T^4 v_w \left(\frac{c_4}{3}\right) \partial_\xi \left(\frac{\delta T}{T}\right). \tag{5.41}$$

We can combine the three expressions in a matrix form, which will be useful for generalization and numerical solutions:

$$4\pi\gamma T^3 \begin{pmatrix} v_w c_2 & v_w c_3 & \frac{c_3}{3} \\ c_3 v_w T & c_4 T v_w & \frac{c_4 T}{3} \\ c_3 T & \frac{c_4 T}{3} & \frac{c_4 v_w T}{3} \end{pmatrix} \times \frac{d}{d\xi} \begin{pmatrix} \delta\mu \\ \frac{-\delta T}{T} \\ \delta v \end{pmatrix}. \tag{5.42}$$

We need to be careful with factors of T and also with additional factors that will be important for the final results of the solutions. Dividing everything by $(2\pi)^3\gamma$ one can define the kinetic matrix A:

$$A\frac{dq}{d\xi} \equiv= \frac{T^3}{2\pi^2} \begin{pmatrix} v_w c_2 & v_w c_3 & \frac{c_3}{3} \\ c_3 T v_w & c_4 T v_w & \frac{c_4 T}{3} \\ c_3 T & \frac{c_4 T}{3} & \frac{c_4 v_w T}{3} \end{pmatrix} \times \frac{d}{d\xi} \begin{pmatrix} \delta\mu \\ \frac{-\delta T}{T} \\ \delta v \end{pmatrix}. \tag{5.43}$$

Now, let us move on to the source terms.

5.4.2 Source terms

By computing the derivatives from equation 5.18, the first derivative of the second term cancels out entirely with the first term of the source, leaving only the second term applied. This leads to:

$$\int \frac{d^3p}{E}(f'_{eq})u^\mu \frac{\partial_\mu m^2}{2}. \tag{5.44}$$

Here, we do not have to deal with the fluctuations, as the source terms are defined against the equilibrium distribution, making the task of taking moments simpler. Thus, the moments of 1, $p^\mu u_\mu$, and $p^\mu \bar{u}_\mu$ are as follows:

$$\int \frac{d^3p}{E}(f'_{eq})\frac{\partial_\mu m^2}{2}, \tag{5.45}$$

$$\int \frac{d^3p\, p^\mu u_\mu}{E}(f'_{eq})\frac{\partial_\mu m^2}{2}, \tag{5.46}$$

$$\int \frac{d^3p\, p^\mu \bar{u}_\mu}{E}(f'_{eq})\frac{\partial_\mu m^2}{2}. \tag{5.47}$$

Using equation 5.23 again and dividing by the factor introduced inside the kinetic matrix we arrive at,

$$S = \frac{1}{(2\pi)^3\gamma}4\pi v_w u^\mu \partial_\mu m^2 \begin{pmatrix} c_1 \\ c_2 T \\ 0 \end{pmatrix}. \tag{5.48}$$

The divergence term can also be linearized, and we find

$$S = \frac{1}{(2\pi)^3\gamma}4\pi v_w u^\mu \gamma(v_w u_\mu + \bar{u}_\mu)\partial_\xi m^2 \begin{pmatrix} c_1 \\ c_2 T \\ 0 \end{pmatrix} = \frac{1}{2\pi^2} v_w \partial_\xi m^2 \begin{pmatrix} c_1 \\ c_2 T \\ 0 \end{pmatrix} \tag{5.49}$$

5.4.3 Collision terms

Now, for the interaction terms (collision terms), our integrals will take the form

$$\text{coll} = \mathcal{C}[f_p] = \frac{1}{2}\sum_{\text{processes}} \int \frac{d^3p d^3k\, d^3p'\, d^3k' \delta}{(2\pi)^9 (E_p) 2E_k\, 2E_{p'}\, 2E_{k'}} |\mathcal{M}_{pk\to p'k'}|^2 (2\pi)^4 \delta^4(p + k - p' - k')\, \mathcal{P}_{pk\to p'k'}, \tag{5.50}$$

To compute this, we will include the annihilation and scattering processes described in figure 22.

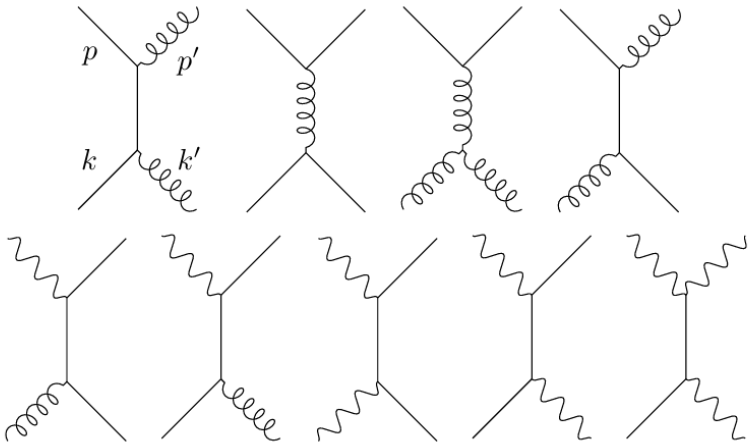

Figure 22 – Diagrams considered in the collision terms of this work. We compute only the leading-log contributions, focusing on t- and u-channel diagrams. The four diagrams in the first row represent processes that change the perturbations of the top quark, namely: double annihilation into gluons, scattering by light quarks, scattering by gluons, and absorption and re-emission of a gluon. The second row represents processes that change the distribution of W bosons, namely: single annihilation (by gluons into quarks and by quarks into gluons), double annihilation into quarks, absorption and re-emission, and scattering by quarks.

5.4.3.1 Example of an annihilation process

We can now compute some collision integrals and take moments to understand this mechanism at first order better.

The integral 5.50 can be solved using standard QFT methods. To better understand the computation of these processes step by step, let us first compute the Feynman diagram for $q\bar{q} \to gg$ using QCD.

The tree-level diagrams that contribute are illustrated in figure 23. As mentioned

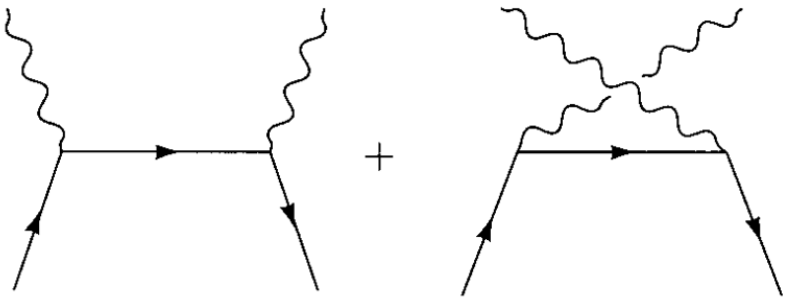

Figure 23 – Diagrams that contribute to $q\bar{q} \to gg$

before, we are working within a leading-log approximation. Therefore, we will only consider

the u- and t-channels, which are the only ones that contribute to the logarithmic terms [56]. Consequently, we will compute only the first two diagrams. Choosing $pk \to p'k'$ and applying the Feynman rules, we can write the amplitudes $\mathcal{M}_1$ and $\mathcal{M}_2$ as follows:

$$\begin{aligned} \mathrm{i}\mathcal{M}_1 &= (\mathrm{i}g)^2 \bar{v}(k) \not{\epsilon}^*(k') \frac{\mathrm{i}(\not{p} - \not{p}')}{(p-p')^2} \not{\epsilon}^*(p') u(p) t^b t^a, \\ \mathrm{i}\mathcal{M}_2 &= (\mathrm{i}g)^2 \bar{v}(k) \not{\epsilon}^*(p') \frac{\mathrm{i}(\not{p} - \not{k}')}{(p-k')^2} \not{\epsilon}^*(k') u(p) t^a t^b. \end{aligned} \tag{5.51}$$

Here, u and $\bar{v}$ describe particles and antiparticles in the process, the ϵ's terms describe the polarizations of the gluons, and we are using the slash notation that represents $\not{p} = \gamma^\mu p_\mu$. We are also going to use the famous Mandelstam variables t, u, s in the rest of the section.

It can be seen that the second diagram can be obtained by simply swapping p' with k'. It is convenient to evaluate these diagrams with initial and final states of definite helicities. By the P and CP symmetry of QCD, there are only two independent processes that could be nonzero: $q_L \bar{q}_R \to g_R g_R$ and $q_L \bar{q}_R \to g_R g_L$. Let's evaluate them for the three diagrams. To begin with, we set up the kinematics:

$$\begin{aligned} p^\mu &= (E, 0, 0, E), \qquad p'^\mu = (E, E\sin\theta, 0, E\cos\theta), \\ k^\mu &= (E, 0, 0, -E), \quad k'^\mu = (E, -E\sin\theta, 0, -E\cos\theta). \end{aligned}$$

Then,

$$u_L(p) = \sqrt{2E}(0,1,0,0), \quad v_L(k) = \sqrt{2E}(1,0,0,0).$$

With this set up, we can write the polarization vectors for the gluons (respecting $\epsilon^\mu \epsilon^*_\mu = -1$ and $k_\mu \epsilon_\mu = 0$):

$$\begin{aligned} \epsilon^*_{L\mu}(p) &= \frac{1}{\sqrt{2}}(0, -\cos\theta, -i, \sin\theta), \quad \epsilon^*_{R\mu}(p) = \frac{1}{\sqrt{2}}(0, -\cos\theta, i, \sin\theta), \\ \epsilon^*_{L\mu}(k') &= \frac{1}{\sqrt{2}}(0, \cos\theta, -i, -\sin\theta), \quad \epsilon^*_{R\mu}(k') = \frac{1}{\sqrt{2}}(0, \cos\theta, i, -\sin\theta). \end{aligned} \tag{5.52}$$

Now, let us compute $i\mathcal{M}_1(q_L \bar{q}_R \to g_R g_R)$:

$$\begin{aligned} \mathrm{i}\mathcal{M}_1(q_L \bar{q}_R \to g_R g_R) = \frac{-\mathrm{i}g^2 E^2 t^b t^a}{t - m_q^2} &(0,0,1,0) \\ &\times (\gamma_1 c_\theta + \gamma_2 i + \gamma_3(-s_\theta)) \times (\gamma_0 + \gamma_3 - \gamma_0 - \gamma_1 s_\theta - \gamma_3 c_\theta) \\ &\times (\gamma_1(-c_\theta) + \gamma_2 i + \gamma_3 s_\theta) \begin{pmatrix} 0 \\ 1 \\ 0 \\ 0 \end{pmatrix}. \end{aligned} \tag{5.53}$$

This simplifies to:

$$
\begin{aligned}
\mathrm{i}\mathcal{M}_1(q_L\bar{q}_R \to g_R g_R) = \frac{-\mathrm{i}g^2E^2t^bt^a}{t}&(0,0,1,0)\\
&\times\begin{pmatrix} 0 & 0 & -s_\theta & 1+c_\theta \\ 0 & 0 & -1+c_\theta & s_\theta \\ s_\theta & -1-c_\theta & 0 & 0 \\ 1-c_\theta & -s_\theta & 0 & 0 \end{pmatrix}\\
&\times\begin{pmatrix} 0 & 0 & 1-c_\theta & -s_\theta \\ 0 & 0 & -s_\theta & -1+c_\theta \\ -1+c_\theta & s_\theta & 0 & 0 \\ s_\theta & 1-c_\theta & 0 & 0 \end{pmatrix}\\
&\times\begin{pmatrix} 0 & 0 & s_\theta & 1-c_\theta \\ 0 & 0 & 1-c_\theta & -s_\theta \\ -s_\theta & -1+c_\theta & 0 & 0 \\ 1+c_\theta & s_\theta & 0 & 0 \end{pmatrix}\begin{pmatrix}0\\1\\0\\0\end{pmatrix}\\
&= -ig^2E^2t^bt^a 2s_\theta(c_\theta-1).
\end{aligned}
\tag{5.54}
$$

Using the relation $t = -2E^2(1-c_\theta)$, we obtain:

$$
\mathrm{i}\mathcal{M}_1(q_L\bar{q}_R \to g_R g_R) = -ig^2t^bt^a s_\theta \frac{t}{t-m_q^2}. \tag{5.55}
$$

Similarly, for $u = -2E^2(1+c_\theta)$, we have:

$$
\mathrm{i}\mathcal{M}_1(q_L\bar{q}_R \to g_R g_R) = ig^2t^bt^a s_\theta \frac{u}{u-m_q^2}. \tag{5.56}
$$

Thus, the total amplitude is:

$$
\mathrm{i}\mathcal{M}(q_L\bar{q}_R \to g_R g_R) = -ig^2\left(t^bt^a\frac{t}{t-m_q^2} - t^at^b\frac{u}{u-m_q^2}\right)\sin\theta. \tag{5.57}
$$

For the other helicities, we have:

$$
\begin{aligned}
\mathrm{i}\mathcal{M}_1(q_L\bar{q}_R \to g_R g_L) &= -ig^2t^bt^a\sin\theta\frac{t}{t-m_q^2},\\
\mathrm{i}\mathcal{M}_2(q_L\bar{q}_R \to g_R g_L) &= -ig^2t^at^b\frac{t}{u-m_q^2}\sin\theta,\\
\mathrm{i}\mathcal{M}_1\left(q_L\bar{q}_R \to g_L g_R\right) &= -\mathrm{i}g^2t^bt^a\sin\theta\frac{u}{u-m_q^2},\\
\mathrm{i}\mathcal{M}_2\left(q_L\bar{q}_R \to g_L g_R\right) &= -\mathrm{i}g^2t^at^b\frac{t}{u-m_q^2}\sin\theta.
\end{aligned}
$$

Therefore,

$$
\mathrm{i}\mathcal{M}\left(q_L\bar{q}_R \to g_R g_L\right) = -\mathrm{i}g^2\left(t^bt^a\frac{t}{t-m_q^2} + t^at^b\frac{t}{u-m_q^2}\right)\sin\theta.
$$

And computing the other two amplitudes:

$$\mathrm{i}\mathcal{M}\left(q_L\bar{q}_R \to g_L g_R\right) = -\mathrm{i}g^2\left(t^b t^a \frac{t}{u-m_q^2} + t^a t^b \frac{u}{t-m_q^2}\right)\sin\theta.$$

The above amplitudes will lead to logarithmic divergences in the limit of massless quarks, $m_q \to 0$, which we will adopt (except for thermal contributions to the masses, which will regulate this divergence). Then clearly the most important term in the expansion is this logarithmic. This motivates us to simplify the analysis by truncating every higher-order term beyond this leading-logarithm. This is called the "leading-log approximation" in the literature, and is the approximation we will adopt here. In this case, one can set $t = u$. This will lead to simpler terms and also simplify $\sin(\theta)$ to unity. Therefore, let's take the average, sum the spins and the helicities, and finally compute $|\mathcal{M}|^2$, making sure to include the factor of two from the initial factor $q_R\bar{q_L}$ and this gives the final result typically quoted in the literature [43]:

$$\begin{aligned}
&\frac{1}{3}\cdot\frac{1}{2^2}\sum_{\text{spin, color}}|\mathcal{M}|^2 \\
&\quad= \frac{1}{12}\cdot 2\cdot g^4\sin^2\theta\Bigg[\left(2\,\mathrm{tr}\left(t^b t^a t^a t^b\right) + 4\,\mathrm{tr}\left(t^b t^a t^b t^a\right) + 2\,\mathrm{tr}\left(t^a t^b t^b t^a\right)\right) \\
&\qquad + 2\left(\mathrm{tr}\left(t^b t^a t^a t^b\right) - 4\,\mathrm{tr}\left(t^b t^a t^b t^a\right) + 2\,\mathrm{tr}\left(t^a t^b t^b t^a\right)\right)\Bigg]\frac{t^2}{(t-m_q^2)^2} \qquad (5.58)\\
&= \frac{1}{12}\cdot 2\cdot g^4\cdot 8\cdot\left(\frac{t^2}{t-m_q^2}\,\mathrm{tr}\left(t^b t^a t^a t^b\right)\right) = \frac{1}{12}\cdot 2\cdot g^4\cdot 8\cdot\left(\frac{t^2}{(t-m_q^2)^2}\cdot\frac{16}{3}\right) = \\
&-\frac{128}{9}\cdot g^4\cdot\left(\frac{st}{(t-m_q^2)^2}\right).
\end{aligned}$$

To solve the traces, we used the properties of $SU(3)$ trace explicitly found in [57] and again applied the leading-log approximation, which turns $t = -2s$. This gives us the final result:

$$|M_{pk\to p'k'}|^2 = -\frac{128}{9}g_s^4\frac{st}{\left(t-m_q^2\right)^2}.$$

The collision term therefore turns into:

$$\begin{aligned}
&\frac{128g_s^4}{9}\int\frac{d^3p}{(2\pi)^3 2E_p}\frac{d^3k}{(2\pi)^3 2E_k}\left[\mu + p^\mu\delta u_\mu - p^\mu u_\mu\left(\frac{\delta T}{T^2}\right)\right]. \\
&\quad\times\int\frac{d^3p'}{(2\pi)^3 2E_{p'}}\frac{d^3k'}{(2\pi)^3 2E_{k'}}\frac{st}{\left(t-m_q^2\right)^2}(2\pi)^4\delta^4\left(p+k-p'-k'\right)\mathcal{P}\left[f_i\right]. \qquad (5.59)
\end{aligned}$$

The entire analysis is performed to linear order in the perturbation, simplifying the population factor as done in [58]. Furthermore, in the leading log approximation, the energy transfer is small, allowing us to approximate

$$\mathcal{P} = f_p f_k \left(1 + f_{p'}\right)\left(1 + f_{k'}\right) \simeq f_p f_k \left(1 + f_p\right)\left(1 + f_k\right). \tag{5.60}$$

By performing the p' and k' integrals first, the δ^4 function can be splitted in the one-dimensional part and 1 three-dimensional part, and the integral over $d^3p'd^3k'$ simplifies to:

$$\begin{aligned}\int_{p'}\int_{k'} = \int \frac{d^3p'\, d^3k'}{(2\pi)^6 4E_{p'}E_{k'}} \frac{-st}{(t-m_q^2)^2}(2\pi)^4\delta(2E_p - 2E_{p'}) \\ \delta^3(2p' - 2p')f_p f_k(1+f_{p'})(1+f_{k'}).\end{aligned} \tag{5.61}$$

Recalling the Mandelstam variables $s = (k'+p')^2 = (p+k)^2$ and $t = (p-p')^2 = (k-k')^2$, the term st inside the integral becomes:

$$t = (p-p')^2 = 2|\vec{p}||\vec{p}\,'|(1-\cos\theta').$$

Here, we used the assumption that the particles in the external legs are massless outside the bubble. Additionally, we can use the identity $s = 4E_{cm}^2 = 2k\cdot p$, as provided by 5.4.3.1. With this, the integral over k' and p' simplifies to:

$$\begin{aligned}\int_{k'}\int_{p'} &= \int \frac{dp'p'^2 d\theta' \sin(\theta')(2\pi)(2k\cdot p)2pp'(1-\cos\theta')\delta(2E_p - 2E_{k'})}{(2\pi)^3 4E_{p'}E_{p'}(2pp'(1-\cos\theta')+m_q^2)^2} \\ &= \int \frac{p'^2 dp' d\theta' \sin(\theta')(2k\cdot p)2pp'(1-\cos\theta')\delta(2E_p - 2E_{p'})}{(2\pi)4E_{p'}E_k(2pp'(1-\cos\theta')+m_q^2)^2}. \qquad (5.62) \\ &= \int \frac{d\theta' \sin(\theta')(2k\cdot p)2pp'(1-\cos\theta')}{(2\pi)4(2pp'(1-\cos\theta')+m_q^2)^2}. \qquad (5.63)\end{aligned}$$

To deal with this angular integral, we will keep only the leading-log term, which is dominant in the limit of $m_q \to 0$. Then, this transforms the angular part θ' integral into

$$\int \frac{d\theta' \sin(\theta')(2k\cdot p)2pp'(1-\cos\theta')}{(2\pi)4(2pp'(1-\cos\theta')+m_q^2)^2} \approx \frac{1}{8\pi}\ln\left(\frac{2k\cdot p}{m_q^2}\right). \tag{5.64}$$

Now, integrating over p and k, a factor of $16\pi^2$ appears in the numerator due to the angular integrals, and the energies can be simplified for each momentum, p and k. Then, the full integral becomes:

$$\frac{2g_s^4}{18\pi^5}\int pk\ln\left(\frac{4pk}{m_q^2}\right)\delta f_p f_k(1+f_p)(1+f_k)\left[\mu + p^\mu \delta u_\mu - p^\mu u_\mu\left(\frac{\delta T}{T^2}\right)\right] dp\, dk. \tag{5.65}$$

We see here the logarithmic divergence in the limit $m_q \to 0$, which we mentioned above. This equation represents the first moment. To factor out the other two types of momentum, we use the approximation [58]:

$$\int p^n \ln\left(\frac{p}{T}\right) f_p(1+f_p) \approx \ln\left(n+\frac{1}{2}\right)\int p^n f_p(1+f_p)\, dp. \tag{5.66}$$

Finally, using Equation (5.25) and taking three moments—1, $p^\mu u_\mu$, and $p^\mu \bar{u}_\mu$—we find the terms of linear order:

$$\Gamma_{\text{annih}} = \frac{2g_s^4}{9\pi^5} \begin{pmatrix} \ln\left(\frac{9T^2}{m^2}\right)\tilde{c}_2^2 T^3 & \ln\left(\frac{15T^2}{m^2}\right)\tilde{c}_2\tilde{c}_3 T^3 & 0 \\ \ln\left(\frac{15T^2}{m^2}\right)\tilde{c}_2\tilde{c}_3 T^4 & \frac{1}{2}\left[\begin{matrix}\ln\left(\frac{21T^2}{m^2}\right)\tilde{c}_2\tilde{c}_4 \\ +\ln\left(\frac{25T^2}{m^2}\right)\tilde{c}_3^2\end{matrix}\right]T^4 & 0 \\ 0 & 0 & \frac{3}{2}\left[\begin{matrix}\ln\left(\frac{21T^2}{m^2}\right)\tilde{c}_2\tilde{c}_4 \\ +\ln\left(\frac{25T^2}{m^2}\right)\tilde{c}_3^2\end{matrix}\right]T^4 \end{pmatrix}.$$

As a final remark regarding dimensions, the goal is to render every equation in our system dimensionless. To achieve this, we divide each equation by T^3, thereby eliminating any additional temperature factors in the second and third rows of the kinetic, source, and collision matrices, as these factors are common to all terms. For the scattering processes, one can follow the steps indicated in [58]. The process is analogous, and is omitted for the sake of brevity.

Let us emphasize that, up to this point, *we have primarily considered first-order fluctuations involving only three moments. However, this can be generalized to arbitrary orders, and even the collision integrals remain exactly solvable at leading log [47]. We implement a numerical code which works to arbitrary order in this momentum expansion, which will be used for obtaining our main results. Any higher-order fluctuation can be handled using the same method we developed, simply by including more moments in the computation and leveraging equations like 5.23 and 5.66, which are essential for building an arbitrary-order framework.* A generic algorithm to implement the results can be found in [47].

5.5 Solving the Boltzmann Equation

Now that we have a clear picture of how each component of the Boltzmann equation behaves, we can proceed to solve it. As argued above, after linearizing in the fluctuations $w^{(i)}$ and taking moments, the equation can be written in matrix form and can be solved using the method of Green's functions. The Boltzmann equation can be written as

$$\frac{dq}{dz} + (A^{-1}\Gamma)q = A^{-1}S \tag{5.67}$$

where

$$S = S_{\text{vec}}\frac{dF}{dz} \tag{5.68}$$

where F is defined has

$$F(z/L_w) = \frac{(m(z))^2}{2T^2} = \frac{m_0^2}{2T^2}\left(\frac{1}{2}\left(1-\tanh\left(\frac{z}{L_w}\right)\right)\right)^2 \tag{5.69}$$

That comes from defining

$$\phi = \frac{\phi_0}{2}\left(1-\tanh\left(\frac{z}{L_w}\right)\right). \tag{5.70}$$

This represents the shape of $\phi(z)$, with z being the bubble's radius.

Defining the term $u = z/L_w$, we get

$$\frac{dq}{du} + L_w(A^{-1}\Gamma)q = A^{-1}S_{\text{vec}}S(u)$$

where

$$S(u) = -\left(\frac{m}{T}\right)^2\left(\frac{1-\tanh(u)}{4\cosh(u)}\right) \tag{5.71}$$

The case with only one perturbation can be solved analytically, but we focus on a generic order of perturbation. The homogeneous solution is trivial:

$$q_{\text{hom}}(u) = \sum_i \alpha_i\chi\exp(-\lambda_i u), \tag{5.72}$$

where α_i and χ_i are the eigenvalues and eigenvectors of the term $L_w(A^{-1}\Gamma)$. To solve the non-homogeneous part, we compute the Green's function G for a source. We know that the solution must go to zero far from the bubble, as the plasma is in equilibrium so the fluctuations vanish. Therefore, the Green's function has the following form:

$$G(u) = \begin{cases} \sum_{\lambda_i>0}\alpha_i\chi_i\exp\left(-\lambda_i u\right), & u>0 \\ \sum_{\lambda_i<0}\alpha_i\chi_i\exp\left(-\lambda_i u\right), & u<0 \end{cases} \tag{5.73}$$

It is important to emphasize that the eigenvalues of $L_w(A^{-1})\Gamma$ represent the thickness of the perturbations around the bubble, i.e., how far the perturbation can propagate. Thus, the solution $q(u)$ is

$$\begin{aligned} q(u) = \left(\chi_i^{-1}\cdot A^{-1}\cdot S_{\text{vec}}\right)\cdot\int_u^\infty du'\sum_{\lambda_i>0}\mathcal{S}(u')\chi_i\exp\left[-\lambda_i(u'-u)\right] \\ -\int_{-\infty}^u du'\sum_{\lambda_i<0}\mathcal{S}(u')\chi_i\exp\left[-\lambda_i(u'-u)\right]. \end{aligned} \tag{5.74}$$

One can also compute the fluctuations for light species in the plasma (small masses in the thermal bath). Importantly, the source terms are absent for the light species by construction, since their masses are not significantly changed during the passage of the bubble. The fluctuations of the light species are only sourced indirectly due to collision terms with the heavy particles. Moreover, the chemical potential of the light species vanishes identically since their particle numbers equilibrate quickly, so the light

elements can be described only through velocity and temperature fluctuations. This means that the corresponding moments of the Boltzmann equation for these species involve a multiplication by $p^\mu u_\mu$ or $p^\mu \bar{u}_\mu$, with a single power of p^μ. Because of this, when summing over the equations for *all* the fluctuations (heavy and light species alike), the sum over the collision terms must vanish. This means that the collision matrix of the light species with tops and weak gauge bosons (collectively denoted as W) satisfy [22]

$$\Gamma_{\text{light},t} = -N_t \Gamma_t \quad \text{and} \quad \Gamma_{\text{light},W} = -N_W \Gamma_W, \tag{5.75}$$

with $N_{t,W}$ the respective number of degrees of freedom, and $\Gamma_{t,W}$ the collision matrix entering the Boltzmann equation for the heavy fluctuations. It's also important to emphasize that the kinetic matrices of the light particles will carry only the moments related with $p^\mu u_\mu$ and $p^\mu \bar{u}_\mu$, leading to a 2x2 matrix, different from the usual 3x3 matrix related with the three moments. Then, for the light species, Boltzmann equation turns into,

$$A_{\text{light}} \cdot q'_{\text{light}} + \Gamma_{\text{light},W} \cdot q_W + \Gamma_{\text{light},t} \cdot q_t = 0. \tag{5.76}$$

With that, the background part of the solution is obtained by integrating $q(u)$:

$$q_{\text{bg}}(u) = \sum_i A^{-1}_{\text{bg}} \left(L_w N_i \Gamma_i\right) \int_\infty^u q_i(u')\, du'. \tag{5.77}$$

With the fluctuations computed, one can apply them into the EOM and chase our final goal: the bubble wall velocity.

6 Computing the wall velocity

By now, we have computed a large set of parameters, but the one that is the focus of this work, namely the bubble wall velocity, still needs to be computed. Let us take care of it.

6.1 Finding the bubble wall velocity v_w

As we discussed, in the bubble wall frame, the observer will only see a steady flow of particles from the plasma into the bubble, and the situation is time-independent. Thus, we can replace $\partial_\nu \to \partial_z$. By modeling the scalar field profile as

$$\phi(z) = \frac{\phi_0}{2}\left(1 - \tanh\frac{z}{L_w}\right), \tag{6.1}$$

the problem reduces to solving the equation of motion

$$\Box\phi + \frac{\partial V(T,\phi)}{\partial\phi} + \sum_i \frac{g_i}{2}\frac{\partial m_i^2}{\partial\phi}\int\frac{d^3p}{(2\pi)^3 E_i}\delta f_i(p,x) = 0. \tag{6.2}$$

for two variables: the wall velocity v_w and the width L_w.

Using equation 5.74, we now have an approximation to solve the fluctuations of the equation of motion. When integrated over the space, this leads to what we call the friction terms. For this, we take two moments of the equation and normalize by the appropriate factors of temperature to obtain a dimensionless quantity, namely

$$\begin{aligned} M_1 &\equiv \frac{1}{T^4}\int_{-\infty}^{\infty}(\text{LHS of eq. (5.16)})\,dz = 0, \\ M_2 &\equiv \frac{1}{T^5}\int_{-\infty}^{\infty}(\text{LHS of eq. (5.16)})(2\phi(z) - \phi_0)\,dz = 0. \end{aligned}$$

However, as the bubble interface crosses the plasma, some particles collide against it and are reflected back, leading to a slightly higher temperature $T_+ > T_n$ immediately ahead of the bubble wall. Since this is the region where the non-equilibrium effects are prominent, we evaluate the above quantities at this temperature T_+ (this justifies our work of chapter 4).

Equations (6.3) can then be written as [44]

$$\begin{aligned} M_1 &\equiv \frac{\Delta V}{T_+^4} + f = 0, \\ M_2 &\equiv \frac{2}{15(L_w T_+)^2}\left(\frac{\phi_0}{T_+}\right)^3 + \frac{W}{T_+^5} + g = 0, \end{aligned} \tag{6.3}$$

where f and g are the terms coming from integration over the non-equilibrium contributions (terms involving δf_i in eq. (5.16)), while

$$\begin{pmatrix} \Delta V \\ W \end{pmatrix} \equiv \int_{-\infty}^{\infty} \frac{\partial V(T_+, \phi)}{\partial \phi} \partial_z \phi \begin{pmatrix} 1 \\ \phi_0 \tanh(z/L_w) \end{pmatrix} dz. \tag{6.4}$$

Note, in particular, that ΔV is (minus) the pressure difference across the wall due to the free energy released by the transition. Then equation M_1 has a simple interpretation: the pressure pushing the wall forward must be counterbalanced by the friction f. On the other hand, the integrand in the definition of W is asymmetric under parity reflections around the origin (due to the $\tanh(z/L_w)$ term), so it can be seen as an overall "stretching" effect that tends to change the wall width. The solution of these equations are the values of v_w and L_w for which these forces are all balanced out.

We implemented a numerical code in Python to solve the Boltzmann equation for the fluctuations $w^{(i)}$ to arbitrary n-th order in momentum expansion 5.13, which can then be plugged back into equation 6.2 to find the friction functions f and g. One can plot equations 6.4 for a fixed parameter while varying the velocity along the x-axis, as shown in Figure 24.The equations (6.4) are then solved for v_w and L_w to find the correct v_w.

It has recently been argued in the literature that, once hydrodynamic effects are taken into account, such as the heating of the plasma ahead of the wall, no non-luminal detonations can be found [59]. This is because the pressure against the wall (i.e., M_1 in eq. (6.4)) blows up as the wall approaches the speed of sound, and suddenly drops when the Jouguet velocity is reached. If the wall has enough energy to overcome the Jouguet threshold, the opposing force will not be able to resist its expansion, and it will inevitably runaway. It is argued that, even if a non-luminal detonation solution exists, a deflagration solution will also exist. Since the wall speed grows from zero up to this stable value, it will stabilize at the deflagration speed. In order to verify this statement, we begin by showing in figure 24 the behavior of the two "forces," M_1 and M_2, as a function of the wall velocity. Here, we consider only top quarks as the heavy particles in the fluid. We perform two analyses: one in which the fluid velocity is taken to be v_w, and another in which it is considered to be v_+. In the former case, there is a discontinuity across the speed of sound due to the behavior of friction. In the latter case, however, the behavior is continuous up to the Jouguet velocity, because v_+ is always smaller than the speed of sound, and the discontinuity in friction is never reached. We will show that, although the overall behavior of M_1 and M_2 changes qualitatively, this choice has little impact on the final result. This is because our model has modest values for the fractional released energy, $\alpha \lesssim 0.01$, and in this case $v_+ \approx v_w$ up to velocities very close to the speed of sound [60].

The left plot in figure 24 corresponds to $M = 700$ GeV. In this case, one notices that the net pressure initially increases until both forces are balanced, after which there is a drop (either across the sound barrier or after the Jouguet velocity, depending on

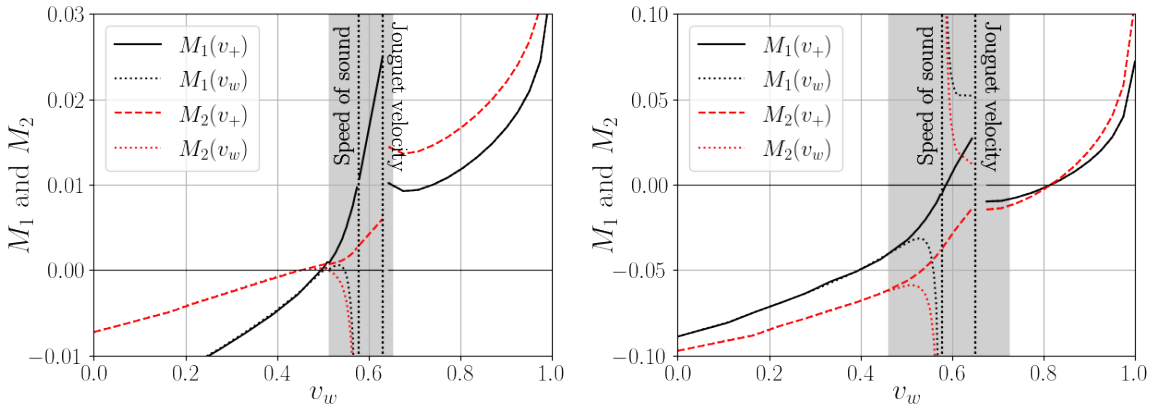

Figure 24 – Pressure difference (M_1) and "stretching force" (M_2) across the wall. The left plot corresponds to $M = 700$ GeV and $L_w T = 7.4266$, with a Jouguet velocity $v_J = 0.630$. In this case, the solution is a deflagration. The right plot corresponds to $M = 630$ GeV and $L_w T = 8.2235$, with a Jouguet velocity $v_J = 0.651$. Here, the solution is a Jouguet detonation. The behavior changes drastically across the sound speed due to the shape of the non-equilibrium friction terms, as shown in figure 24 and discussed in depth in ref. [47]. Across the Jouguet velocity, there is another jump, this time due to hydrodynamical effects, as the expansion is now a detonation, and there is no heating of the plasma in front of the wall. In the shaded region, we expect the linearization procedure of the Boltzmann equation to break down.

whether we consider v_w or v_+). Beyond the Jouguet velocity, the non-equilibrium friction dominates, and the pressure difference is not enough to push the wall at such high velocities, leaving only one solution corresponding to a deflagration. Notice that the point where $M_1 = M_2 = 0$ is approximately the same, whether we use v_w or v_+ as the fluid velocity (there will be a slight change in the wall width L_w that solves these equations as well; here, we plotted for the value L_w that satisfies both equations using v_w as the fluid velocity). The right panel, on the other hand, corresponds to $M = 630$ GeV. In this case, for subsonic walls, the friction is never enough to counterbalance the pressure difference, and the only solution is a detonation. Again, by using v_+ as the velocity ahead of the wall, both M_1 and M_2 continue to grow and cross the x-axis at some point in the deflagration regime, but *not simultaneously*.

One could then expect to find non-luminal detonations as the only solutions in this case. In the shaded grey region, we show the area where we expect a breakdown of our linearization procedure for the Boltzmann equation, which can be estimated to occur when [47]

$$\frac{\alpha}{X_-^2} \gtrsim 1 \quad \text{(breakdown of linearization procedure)}. \tag{6.5}$$

with X_- defined in eq. (4.20).

Figure 25 corroborates the above expectation, showing the wall velocity for varying cutoff scales M in the case where only top quarks are considered heavy. The grey shaded

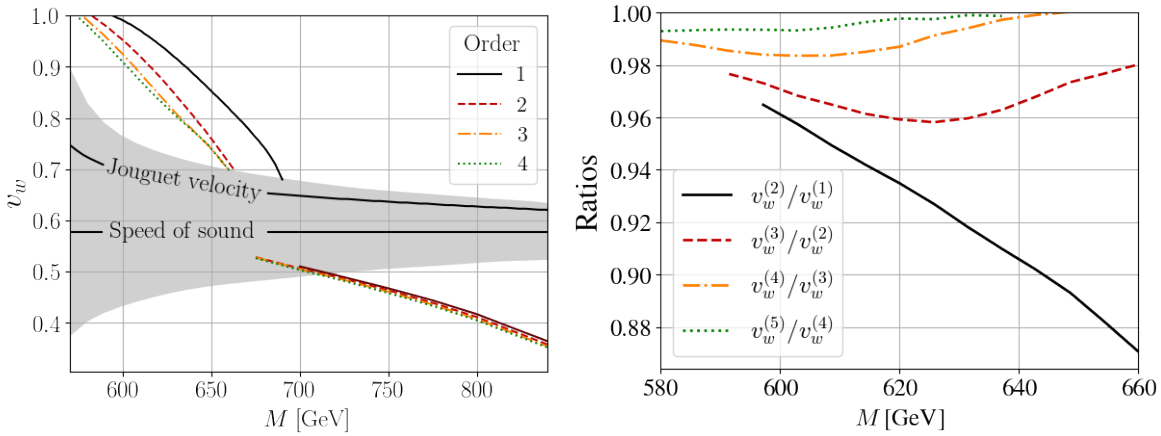

Figure 25 – (Left) Solutions for the bubble wall velocity as a function of the mass scale M, including only top quarks as heavy species in the plasma. The shaded region corresponds to the breakdown of the linearization procedure, so solutions in this region should be interpreted with caution. (Right) Ratio of $v_w^{(i+1)}/v_w^{(i)}$, where $v_w^{(i)}$ is the solution at the i-th order in the fluid expansion. Notice that the solutions converge quickly, as the ratios approach unity.

region corresponds to the breakdown of the validity of the linearization procedure in the Boltzmann equation. This means that, outside the shaded region, our procedure is well under control and the results are trustworthy. It is noticed that for large values of the cutoff M, one approaches the decoupling limit, the transition becomes weaker, and only deflagration solutions exist. But as we decrease M, the transition becomes stronger, and only non-luminal detonations are obtainable in this approach. Further investigation is necessary, however, to check whether other deflagration solutions might appear once we improve the linearization procedure and reduce or altogether remove the grey shaded band.

Finally, we have verified that these results are essentially unchanged whether we use v_w or v_+ as the fluid velocity ahead of the bubble, in agreement with the expectations discussed above. We also show in the right panel of figure 25 the ratio of velocities in the detonation regime, computed at two consecutive orders in the expansion of eq. (5.12). Notice that the ratio approaches unity as we increase the order of the expansion, indicating that the expansion converges quickly. It is also noteworthy that the inclusion of second-order effects may reduce the wall velocity by a factor of $\mathcal{O}(10\%)$ compared to a first-order calculation, highlighting the inappropriateness of the perfect fluid *Ansatz*.

Let us now consider the case where the W's and Z's are also included as heavy species. The results in this case are qualitatively different, as seen in figure 26. If we truncate the fluid expansion at first order, i.e., consider a perfect fluid only, we obtain similar results to the previous case: deflagrations at large M and detonations for low enough cutoff (strong enough transitions). However, as higher-order terms are included,

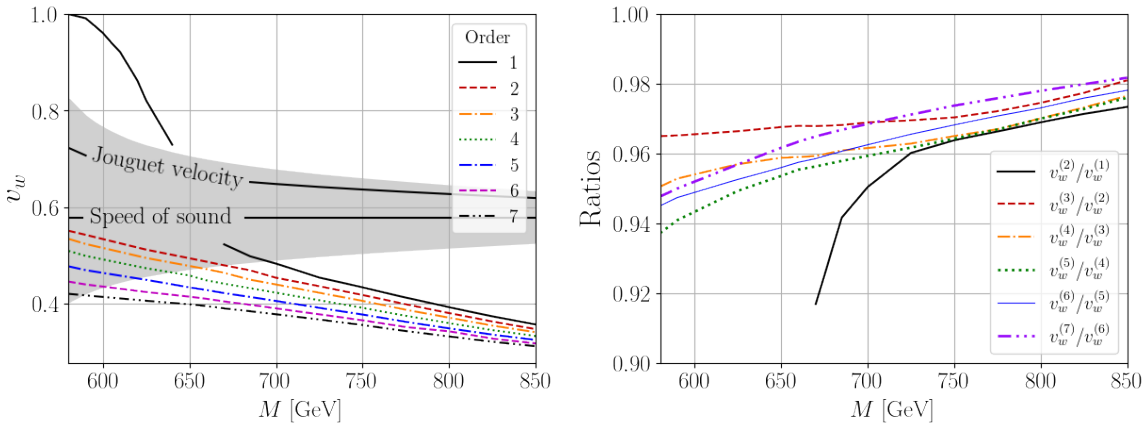

Figure 26 – (Left) Solutions for the bubble wall velocity as a function of the mass scale M, including top quarks, W's, and Z's as heavy species. As in figure 25, the shaded region corresponds to the breakdown of the linearization procedure. (Right) Ratio of solutions at two consecutive orders in the fluid expansion. The convergence is slower here compared to the top-only case, but it still occurs.

detonation solutions become untenable. This shows that the inclusion of higher-order terms in the fluid expansion can lead to qualitatively different results compared to truncating the expansion at three fluctuations. Moreover, our findings corroborate recent results in [51,59], which suggest that consistent solutions are deflagrations. However, the impossibility of non-luminal detonations might not be a general statement and could depend on the particle content of the theory.

The right panel of figure 26 illustrates the convergence tendency of the momentum expansion. We emphasize that such convergence is expected for any reasonably well-behaved function, since eq. (5.12) is analogous to an expansion in 4-dimensional spherical harmonics [54]. However, figure 26 shows that, in the presence of gauge bosons, this convergence is slower than what we observed when only top quarks were considered. This can be understood by noting that the expansion parameter is $\mathcal{O}(D/L)$, where D is the diffusion length of the plasma particles and L is the wall width [58]. For top quarks, $D_{\text{top}} \simeq 2.9/T$, whereas for gauge bosons, $D_{\text{W}} \simeq 5.5/T$, which is almost twice as large [58,61].

7 Conclusion and final remarks

Determining the velocity of bubble expansion during a first order phase transition is essential for an accurate estimate of the relics stemming from such a process. There have been many recent developments in the literature in this direction, including alternative ways to model non-equilibrium dynamics in the plasma. In this work we study the behaviour of the wall velocity when the friction is evaluated with the so-called "extended fluid *Ansatz*". In this approach the non-equilibrium distribution functions have the same functional shape as the equilibrium ones, but while the former depends only on a single power of energy and momentum, the latter instead includes arbitrary powers of a momentum expansion. Since this amounts to an expansion in 4d spherical harmonics, one expects that any reasonably well behaved function could be approximated this way.

We then solve the Boltzmann equation in this approach and compute the fluctuations away from equilibrium, leading to the friction terms. In our solution, we perform a linearization procedure which does not always hold. However, we can establish a criterion for its validity, and can then have an adequate estimate of the reliability of our methods.

Our main result is that the inclusion of higher order terms in the momentum expansion of the fluid *Ansatz* are typically very relevant, and in some cases may even turn a detonation solution into a deflagration. For a Standard Model particle content in the plasma, considering the W and Z bosons and the top quark as heavy species, no detonations are found once we include terms beyond the perfect fluid *Ansatz*, corroborating recent findings in the literature [51, 59]. However, this conclusion could be heavily dependent on the particle content of the plasma. We illustrate this statement by also analysing a situation where only top quarks are included as heavy species. In this case the overall picture changes and non-luminal detonations seem to be the only viable solutions for sufficiently small M. However, more investigation is needed to check whether deflagrations could be viable solutions in this range once we improve the linearization procedure. Moreover, in this detonation regime the inclusion of higher order terms in the fluid *Ansatz* is quantitatively important, as the difference to the perfect fluid result may be a factor of $\mathcal{O}(10\%)$ or higher. On a final note, we have checked that the momentum expansion tends to converge, albeit slowly when gauge bosons are included in the picture because of their larger diffusion length compared to the top quarks.

It would be interesting to investigate how the result would be impacted should we include the spatial dependence of the coefficients appearing in the Boltzmann system. Similarly, one could also include the spatial dependence of the temperature profile across the bubble wall, which varies from T_- behind the wall to T_+ ahead of it. We did this in

the recent paper. [62].

Besides this important result, in this dissertation we provided a detailed analysis of the behavior of various aspects of a first-order electroweak phase transition and explained the entire process of calculating the most important parameters for the theoretical power spectra. This field lacks a single, comprehensive, and detailed study, and often the computations are fragmented and unclear. Therefore, in addition to the interesting results we obtained, this dissertation could serve as a valuable resource for other scientists in training in the discussed field.

Bibliography

[1] Ryden, B.S.: *Introduction to Cosmology*. Addison-Wesley, 2003, ISBN 9780805389128. https://books.google.com.br/books?id=z27vAAAAMAAJ. Citado na página 9.

[2] Mukhanov, V.: *Physical Foundations of Cosmology*. Cambridge University Press, Oxford, 2005, ISBN 978-0-521-56398-7. Citado 2 vezes nas páginas 10 e 27.

[3] Weinberg, Steven: *Cosmology*. 2008, ISBN 978-0-19-852682-7. Citado na página 10.

[4] Abbott, B. P. *et al.*: *Observation of Gravitational Waves from a Binary Black Hole Merger*. Phys. Rev. Lett., 116(6):061102, 2016. Citado 2 vezes nas páginas 10 e 11.

[5] Abbott, B. P. *et al.*: *GWTC-1: A Gravitational-Wave Transient Catalog of Compact Binary Mergers Observed by LIGO and Virgo during the First and Second Observing Runs*. Phys. Rev. X, 9(3):031040, 2019. Citado 2 vezes nas páginas 10 e 11.

[6] Abbott, R. *et al.*: *GWTC-2.1: Deep Extended Catalog of Compact Binary Coalescences Observed by LIGO and Virgo During the First Half of the Third Observing Run*. agosto 2021. Citado 2 vezes nas páginas 10 e 11.

[7] Abbott, R. *et al.*: *GWTC-3: Compact Binary Coalescences Observed by LIGO and Virgo During the Second Part of the Third Observing Run*. novembro 2021. Citado 2 vezes nas páginas 10 e 11.

[8] Agazie, Gabriella *et al.*: *The NANOGrav 15 yr Data Set: Evidence for a Gravitational-wave Background*. Astrophys. J. Lett., 951(1):L8, 2023. Citado 2 vezes nas páginas 11 e 30.

[9] Anderson, Greg W. e Lawrence J. Hall: *Electroweak phase transition and baryogenesis*. Phys. Rev. D, 45:2685–2698, Apr 1992. https://link.aps.org/doi/10.1103/PhysRevD.45.2685. Citado na página 11.

[10] Caprini, Chiara e Daniel G. Figueroa: *Cosmological Backgrounds of Gravitational Waves*. Class. Quant. Grav., 35(16):163001, 2018. Citado na página 11.

[11] Hindmarsh, Mark B., Marvin Lüben, Johannes Lumma e Martin Pauly: *Phase transitions in the early universe*. SciPost Phys. Lect. Notes, 24:1, 2021. Citado 2 vezes nas páginas 11 e 42.

[12] Athron, Peter, Csaba Balázs, Andrew Fowlie, Lachlan Morris e Lei Wu: *Cosmological phase transitions: from perturbative particle physics to gravitational waves*. maio 2023. Citado na página 11.

[13] Caprini, Chiara, Mark Hindmarsh, Stephan Huber, Thomas Konstandin, Jonathan Kozaczuk, Germano Nardini, Jose Miguel No, Antoine Petiteau, Pedro Schwaller, Géraldine Servant e David J. Weir: *Science with the space-based interferometer eLISA. II: gravitational waves from cosmological phase transitions*. Journal of Cosmology and Astroparticle Physics, 2016(04):001–001, abril 2016, ISSN 1475-7516. `http://dx.doi.org/10.1088/1475-7516/2016/04/001`. Citado 5 vezes nas páginas 11, 29, 33, 34 e 36.

[14] Caprini, Chiara *et al.*: *Detecting gravitational waves from cosmological phase transitions with LISA: an update*. JCAP, 03:024, 2020. Citado na página 11.

[15] Arcadi, Giorgio, Glauber C. Dorsch, Jacinto P. Neto, Farinaldo S. Queiroz e Y. M. Oviedo-Torres: *Probing a Dark Sector with Collider Physics, Direct Detection, and Gravitational Waves*. julho 2023. Citado na página 11.

[16] Konstandin, Thomas: *Quantum Transport and Electroweak Baryogenesis*. Phys. Usp., 56:747–771, 2013. Citado na página 11.

[17] Morrissey, David E. e Michael J. Ramsey-Musolf: *Electroweak baryogenesis*. New J. Phys., 14:125003, 2012. Citado na página 11.

[18] Azatov, Aleksandr, Miguel Vanvlasselaer e Wen Yin: *Dark Matter production from relativistic bubble walls*. JHEP, 03:288, 2021. Citado na página 11.

[19] Baldes, Iason, Yann Gouttenoire e Filippo Sala: *Hot and heavy dark matter from a weak scale phase transition*. SciPost Phys., 14:033, 2023. Citado na página 11.

[20] Jiang, Siyu, Fa Peng Huang e Chong Sheng Li: *Hydrodynamic effects on the filtered dark matter produced by a first-order phase transition*. Phys. Rev. D, 108(6):063508, 2023. Citado na página 11.

[21] Chun, Eung Jin, Tomasz P. Dutka, Tae Hyun Jung, Xander Nagels e Miguel Vanvlasselaer: *Bubble-assisted leptogenesis*. JHEP, 09:164, 2023. Citado na página 11.

[22] Dorsch, Glauber C., Stephan J. Huber e Thomas Konstandin: *A sonic boom in bubble wall friction*. JCAP, 04(04):010, 2022. Citado 3 vezes nas páginas 11, 50 e 64.

[23] Langacker, Paul: *The standard model and beyond*. 2010. Citado na página 18.

[24] Mustafa, Munshi G.: *An introduction to thermal field theory and some of its application*. The European Physical Journal Special Topics, 232(9):1369–1457, julho 2023, ISSN 1951-6401. `http://dx.doi.org/10.1140/epjs/s11734-023-00868-8`. Citado 2 vezes nas páginas 18 e 22.

[25] Camargo-Molina, José Eliel, Rikard Enberg e Johan Löfgren: *A new perspective on the electroweak phase transition in the Standard Model Effective Field Theory*. Journal of High Energy Physics, 2021(10), outubro 2021, ISSN 1029-8479. http://dx.doi.org/10.1007/JHEP10(2021)127. Citado na página 19.

[26] Alvim, Maria Clara: *Mecanismo de Higgs e Transição de Fase no Universo Primordial*. UFMG, 2024. Citado na página 24.

[27] Hohenberg, P.C. e A.P. Krekhov: *An introduction to the Ginzburg–Landau theory of phase transitions and nonequilibrium patterns*. Physics Reports, 572:1–42, abril 2015, ISSN 0370-1573. http://dx.doi.org/10.1016/j.physrep.2015.01.001. Citado na página 25.

[28] Mukhanov, Viatcheslav: *Physical Foundations of Cosmology*. Cambridge Univ. Press, Cambridge, 2005. https://cds.cern.ch/record/991646. Citado na página 26.

[29] Athron, Peter, Csaba Balázs e Lachlan Morris: *Supercool subtleties of cosmological phase transitions*. Journal of Cosmology and Astroparticle Physics, 2023(03):006, março 2023, ISSN 1475-7516. http://dx.doi.org/10.1088/1475-7516/2023/03/006. Citado na página 29.

[30] Giese, Felix, Thomas Konstandin e Jorinde van de Vis: *Model-independent energy budget of cosmological first-order phase transitions—A sound argument to go beyond the bag model*. Journal of Cosmology and Astroparticle Physics, 2020(07):057–057, julho 2020, ISSN 1475-7516. http://dx.doi.org/10.1088/1475-7516/2020/07/057. Citado na página 29.

[31] Carroll, S.M.: *Spacetime and Geometry*. Cambridge University Press, 2019, ISBN 9781108488396. https://books.google.com.br/books?id=PTGdDwAAQBAJ. Citado 2 vezes nas páginas 30 e 31.

[32] Weisberg, Joel M, Joseph H Taylor e Lee A Fowler: *Gravitational waves from an orbiting pulsar*. Scientific American, 245(4):74–83, 1981. Citado na página 30.

[33] Pustovoit, V I: *On the direct detection of gravitational waves*. Physics-Uspekhi, 59(10):1034, oct 2016. https://dx.doi.org/10.3367/UFNe.2016.03.037900. Citado na página 30.

[34] Maggiore, Michele: *Gravitational Waves. Vol. 1: Theory and Experiments*. Oxford University Press, 2007, ISBN 978-0-19-171766-6, 978-0-19-852074-0. Citado 3 vezes nas páginas 31, 32 e 35.

[35] Izumi, Kiwamu e Masa Katsu Fujimoto: *A back-linked Fabry–Pérot interferometer for space-borne gravitational wave observations*. Progress of Theoretical and Experimental

Physics, 2021(7), maio 2021, ISSN 2050-3911. http://dx.doi.org/10.1093/ptep/ptab067. Citado na página 32.

[36] Jinno, Ryusuke e Masahiro Takimoto: *Gravitational waves from bubble dynamics: beyond the envelope*. Journal of Cosmology and Astroparticle Physics, 2019(01):060–060, janeiro 2019, ISSN 1475-7516. http://dx.doi.org/10.1088/1475-7516/2019/01/060. Citado na página 33.

[37] Kamionkowski, Marc, Arthur Kosowsky e Michael S. Turner: *Gravitational radiation from first-order phase transitions*. Physical Review D, 49(6):2837–2851, março 1994, ISSN 0556-2821. http://dx.doi.org/10.1103/PhysRevD.49.2837. Citado na página 33.

[38] Huber, Stephan J e Thomas Konstandin: *Gravitational wave production by collisions: more bubbles*. Journal of Cosmology and Astroparticle Physics, 2008(09):022, setembro 2008, ISSN 1475-7516. http://dx.doi.org/10.1088/1475-7516/2008/09/022. Citado na página 33.

[39] Kosowsky, Arthur, Andrew Mack e Tinatin Kahniashvili: *Gravitational radiation from cosmological turbulence*. Physical Review D, 66(2), julho 2002, ISSN 1089-4918. http://dx.doi.org/10.1103/PhysRevD.66.024030. Citado na página 34.

[40] Caprini, Chiara, Mikael Chala, Glauber C. Dorsch, Mark Hindmarsh, Stephan J. Huber, Thomas Konstandin, Jonathan Kozaczuk, Germano Nardini, Jose Miguel No, Kari Rummukainen, Pedro Schwaller, Geraldine Servant, Anders Tranberg e David J. Weir: *Detecting gravitational waves from cosmological phase transitions with LISA: an update*. Journal of Cosmology and Astroparticle Physics, 2020(03):024–024, março 2020, ISSN 1475-7516. http://dx.doi.org/10.1088/1475-7516/2020/03/024. Citado na página 34.

[41] Ellis, John, Marek Lewicki, José Miguel No e Ville Vaskonen: *Gravitational wave energy budget in strongly supercooled phase transitions*. Journal of Cosmology and Astroparticle Physics, 2019(06):024–024, junho 2019, ISSN 1475-7516. http://dx.doi.org/10.1088/1475-7516/2019/06/024. Citado na página 34.

[42] European Space Agency (ESA): *LISA - Laser Interferometer Space Antenna*, 2025. https://www.esa.int/Science_Exploration/Space_Science/LISA, Acessado em: 6 março 2025. Citado 2 vezes nas páginas 35 e 36.

[43] Moore, C J, R H Cole e C P L Berry: *Gravitational-wave sensitivity curves*. Classical and Quantum Gravity, 32(1):015014, dezembro 2014, ISSN 1361-6382. http://dx.doi.org/10.1088/0264-9381/32/1/015014. Citado 3 vezes nas páginas 36, 37 e 60.

[44] Konstandin, Thomas, Germano Nardini e Ingo Rues: *From Boltzmann equations to steady wall velocities*. JCAP, 09:028, 2014. Citado 2 vezes nas páginas 38 e 65.

[45] Dolan, L. e R. Jackiw: *Symmetry behavior at finite temperature*. Phys. Rev. D, 9:3320–3341, Jun 1974. https://link.aps.org/doi/10.1103/PhysRevD.9.3320. Citado na página 39.

[46] Espinosa, Jose R., Thomas Konstandin, Jose M. No e Geraldine Servant: *Energy Budget of Cosmological First-order Phase Transitions*. JCAP, 06:028, 2010. Citado 4 vezes nas páginas 42, 43, 44 e 45.

[47] Dorsch, Glauber C., Stephan J. Huber e Thomas Konstandin: *On the wall velocity dependence of electroweak baryogenesis*. JCAP, 08:020, 2021. Citado 3 vezes nas páginas 42, 62 e 67.

[48] Giese, Felix, Thomas Konstandin e Jorinde van de Vis: *Model-independent energy budget of cosmological first-order phase transitions—A sound argument to go beyond the bag model*. JCAP, 07(07):057, 2020. Citado 3 vezes nas páginas 42, 43 e 44.

[49] Steinhardt, Paul Joseph: *Relativistic Detonation Waves and Bubble Growth in False Vacuum Decay*. Phys. Rev. D, 25:2074, 1982. Citado na página 43.

[50] Leitao, Leonardo e Ariel Megevand: *Spherical and non-spherical bubbles in cosmological phase transitions*. Nucl. Phys. B, 844:450–470, 2011. Citado na página 44.

[51] Lewicki, Marek, Marco Merchand e Mateusz Zych: *Electroweak bubble wall expansion: gravitational waves and baryogenesis in Standard Model-like thermal plasma*. JHEP, 02:017, 2022. Citado 3 vezes nas páginas 45, 69 e 70.

[52] Stefanucci, Gianluca e Robert van Leeuwen: *Nonequilibrium Many-Body Theory of Quantum Systems: A Modern Introduction*. Cambridge University Press, Cambridge, 2013. Citado na página 48.

[53] Konstandin, T: *Quantum transport and electroweak baryogenesis*. Physics-Uspekhi, 56(8):747–771, agosto 2013, ISSN 1468-4780. http://dx.doi.org/10.3367/UFNe.0183.201308a.0785. Citado na página 48.

[54] De Groot, S. R.: *Relativistic Kinetic Theory. Principles and Applications*. 1980. Citado 2 vezes nas páginas 50 e 69.

[55] Piattella, Oliver: *Lecture Notes in Cosmology*. Springer International Publishing, 2018, ISBN 9783319955704. http://dx.doi.org/10.1007/978-3-319-95570-4. Citado na página 53.

[56] Arnold, Peter, Guy David Moore e Laurence G Yaffe: *Transport coefficients in high temperature gauge theories (I): leading-log results*. Journal of High Energy Physics, 2000(11):001–001, novembro 2000, ISSN 1029-8479. http://dx.doi.org/10.1088/1126-6708/2000/11/001. Citado na página 58.

[57] Haber, Howard: *Useful relations among the generators in the defining and adjoint representations of SU(N)*. SciPost Physics Lecture Notes, janeiro 2021, ISSN 2590-1990. http://dx.doi.org/10.21468/SciPostPhysLectNotes.21. Citado na página 60.

[58] Moore, Guy D. e Tomislav Prokopec: *How fast can the wall move? A Study of the electroweak phase transition dynamics*. Phys. Rev. D, 52:7182–7204, 1995. Citado 4 vezes nas páginas 60, 61, 62 e 69.

[59] Cline, James M., Avi Friedlander, Dong Ming He, Kimmo Kainulainen, Benoit Laurent e David Tucker-Smith: *Baryogenesis and gravity waves from a UV-completed electroweak phase transition*. Phys. Rev. D, 103(12):123529, 2021. Citado 3 vezes nas páginas 66, 69 e 70.

[60] Konstandin, Thomas e Jose M. No: *Hydrodynamic obstruction to bubble expansion*. JCAP, 02:008, 2011. Citado na página 66.

[61] Joyce, Michael, Tomislav Prokopec e Neil Turok: *Nonlocal electroweak baryogenesis. Part 2: The Classical regime*. Phys. Rev. D, 53:2958–2980, 1996. Citado na página 69.

[62] Dorsch, Gláuber C., Thomas Konstandin, Enrico Perboni e Daniel A. Pinto: *Non-singular solutions to the Boltzmann equation with a fluid Ansatz*, 2024. https://arxiv.org/abs/2412.09266. Citado na página 71.